Check for updates

ADVANCED FUNCTIONAL MATERIALS
www.afm-journal.de

Enhancing CoFe Catalysts with V_2CT_X MXene-Derived Materials for Anion Exchange Membrane Electrolyzers

*Can Kaplan, Karuppasamy Dharmaraj, Thorsten Schultz, Leiqiang Qin, Ningjun Chen, Danielle A. Douglas-Henry, Bastian Schmiedecke, Merve Buldu-Akturk, Axel Zuber, Iris Dorbandt, Maximilian Reinhardt, Yael Rodriguez-Ayllon, Yan Lu, Valeria Nicolosi, Norbert Koch, Johanna Rosen, and Michelle P. Browne**

Herein, the synthesis and characterization of $Co_{0.66}Fe_{0.34}$ layered double hydroxides (LDH) derived from pure and vacancy-engineered V_2CT_x MXenes and their use as electrocatalysts for the oxygen evolution reaction (OER) is reported. Two distinct MXene materials are investigated: pristine V_2CT_x and $V_{1.8}CT_x$ containing 10% vanadium vacancies. Through systematic variation of the MXene content (17–75 wt.%), it demonstrates that the utilization of MXenes significantly enhances OER activity compared to pure $Co_{0.66}Fe_{0.34}$. The vacancy-engineered composite $Co_{0.66}Fe_{0.34}$@$V_{1.8}CT_x$ achieved superior performance with an overpotential of 304 mV at 10 mA cm^{-2} (CFVv75), compared to 317 mV for the best-performing V_2CT_x MXene composite (CFV33). In situ X-Ray absorption spectroscopy revealed the formation of highly oxidized Co (i.e., Co(III) and Co(IV)) species during OER, while also indicating irreversible oxidation of vanadium to V(V). Despite partial vanadium leaching, both materials demonstrated excellent stability over 12 h of operation at 100 mA cm^{-2}. Notably, CFVv75 showed superior initial performance under practical anion exchange membrane electrolyzer conditions, operating at cell voltages of 100 mV lower than the pure $Co_{0.66}Fe_{0.34}$. This work demonstrates the potential of vacancy engineering and materials discovery using MXene materials for enhancing electrocatalytic performance and provides insights into the dynamic evolution of these materials under operating conditions.

1. Introduction

Water splitting, a pivotal process in green energy technologies, relies critically on the oxygen evolution reaction (OER) as a fundamental electrochemical transformation. The OER represents a significant bottleneck in water electrolysis due to its inherently sluggish kinetics and high activation energy, necessitating the development of advanced electrocatalysts that can efficiently drive this reaction with minimal energy losses.[1] The search for low-cost, stable, and high-performance OER catalysts remains a crucial challenge in realizing economically viable green hydrogen production technologies.

Cobalt-iron (CoFe) alloys have gained significant attention as promising catalysts for the OER due to their remarkable catalytic activity, earth abundance, and cost-effectiveness.[2] Cobalt, renowned for its excellent OER activity in alkaline media, can benefit from the addition of iron, which is suggested to enhance catalytic

C. Kaplan, K. Dharmaraj, B. Schmiedecke, M. Buldu-Akturk, A. Zuber, I. Dorbandt, M. Reinhardt, M. P. Browne
Helmholtz Young Investigator Group Electrocatalysis: Synthesis to Devices
Helmholtz-Zentrum Berlin für Materialien und Energie
12489 Berlin, Germany
E-mail: michelle.browne@helmholtz-berlin.de

T. Schultz, N. Koch
Helmholtz-Zentrum Berlin für Materialien und Energie GmbH
14109 Berlin, Germany

The ORCID identification number(s) for the author(s) of this article can be found under https://doi.org/10.1002/adfm.202503842

© 2025 The Author(s). Advanced Functional Materials published by Wiley-VCH GmbH. This is an open access article under the terms of the Creative Commons Attribution License, which permits use, distribution and reproduction in any medium, provided the original work is properly cited.

DOI: 10.1002/adfm.202503842

T. Schultz, N. Koch
Institut für Physik & CSMB
Humboldt-Universität zu Berlin
12489 Berlin, Germany

L. Qin, N. Chen, J. Rosen
Materials Design Division
Department of Physics
Chemistry and Biology (IFM)
Linköping University
Linköping 58183, Sweden

D. A. Douglas-Henry, V. Nicolosi
School of Chemistry
CRANN and AMBER Research Centres
Trinity College Dublin
College Green
Dublin D02 PN40, Ireland

performance by optimizing the electronic structure and promoting the adsorption and desorption of oxygen intermediates.[3] CoFe layered double hydroxides (LDHs), have emerged as a particularly promising subgroup of CoFe materials for the OER in alkaline media.[4] With their brucite-like layered architecture LDHs offer unique structural advantages, providing multiple active sites and facilitating ion exchange processes. Their general composition $[M^{2+}_{1-x}M^{3+}_{x}(OH)_2]^{x+}[A_{x/n}]^{n-} \cdot mH_2O$ allows for significant compositional and structural tunability, making LDHs attractive candidates for electrocatalytic applications.[5]

However, LDHs, including CoFe-LDHs, conventionally suffer from limited electronic conductivity, which constrains their overall electrocatalytic performance.[6] The charge transfer within these materials primarily occurs through metal cation interactions, resulting in inherently poor electrical conductivity.[7] This fundamental limitation has prompted researchers to explore strategies for enhancing the electronic properties of LDH-based electrocatalysts. One such strategy comprises the introduction of conductive additives such as carbon nanotubes,[8] graphene oxide[9] and mesoporous carbon[10] creating composite materials. However, carbon-based additives are prone to corrosion under potentials relevant for OER and the associated anodic current can confound the interpretation of OER activity.[11]

MXenes have recently emerged as exceptional support materials, offering a unique combination of high electronic conductivity (8000–20000 S cm^{-1}),[12] hydrophilicity, and versatile surface chemistry.[13] Their hexagonal structure, derived from MAX phases through selective etching, provides surface terminations that can serve as critical anchoring points for catalytically active species.[14] Among the numerous possible elemental combinations arising from the formula $M_{n+1}X_nT_x$, titanium carbide ($Ti_3C_2T_x$) was the first successfully synthesized MXene and as such, naturally a focal point of research as a support material for catalysts.[15] For instance recently, we showed that combining cobalt oxide/hydroxide with $Ti_3C_2T_x$ promoted the formation of Co-LDH on the MXene surface and resulted in a more OER active catalyst showing an OER overpotential of 387 mV at 10 mA cm^{-2}.[16] Chemical functionalization of the MXene with Co oxide/hydroxide proved to be more effective than physical mixing of the components. However, the long-term stability of the materials reported in this study were poor. In another study, Hao et al. demonstrated that a combination of CoFe-LDH with $Ti_3C_2T_x$ nanosheets significantly outperformed the pure LDH and other conductive supports, achieving an overpotential of 319 mV at 10 mA cm^{-2}.[17] The growth of CoFe-LDH on $Ti_3C_2T_x$ prevented aggregation, maximized the exposure of active edge sites and improved the conductivity of the catalyst layer.

Y. Rodriguez-Ayllon, Y. Lu
Institute of Electrochemical Energy Storage
Helmholtz-Zentrum Berlin für Materialien und Energie
Hahn-Meitner-Platz 1, 14109 Berlin, Germany
Y. Rodriguez-Ayllon, Y. Lu
Institute for Technical and Environmental Chemistry
Friedrich-Schiller-Universität Jena and Helmholtz Institute for Polymers in Energy Applications (HIPOLE Jena)
Philosophenweg 7b, 07743 Jena, Germany

While not as extensively explored as $Ti_3C_2T_x$, recent studies suggest that V_2CT_x has even greater potential as a support for OER catalysts.[18] In a theoretical and experimental study, Zhao et al. demonstrated that V_2CT_x outperforms other MXenes, i.e., $Ti_3C_2T_x$, and Nb_2CT_x, for the OER when used as a support for Co single atoms.[18a] Their DFT calculations revealed that the V_2CT_x composites had the lowest energy barrier in the rate determining step of the OER, accelerating its reaction kinetics. Moreover, the vanadium atoms in the V_2CT_x structure increased the total density of states (DOS) around the Fermi level for Co@V_2CT_x compared to Co@Nb_2CT_x and Co@$Ti_3C_2T_x$. This increased electron cloud distribution resulted in greater electroconductivity, further enhancing the overall catalytic performance. More recently, Schmiedecke et al. reported that a CuCo@V_2CT_x composite achieved 285 mV at 10 mA cm^{-2}, greatly outperforming the pure CuCo and a comparable $CuCo_2O_4$@$Ti_3C_2T_x$ material.[15d,18b] The improvement was attributed to the strong metal-support interactions between CuCo and V_2CT_x MXene, which facilitated efficient electron transfer.

While MXene materials are generally susceptible to oxidation, which is typically considered a limitation, vanadium carbide MXenes present an intriguing exception. In a recent study Schmiedecke et al. demonstrated that composite materials based on oxidized V_2CT_x exhibited enhanced OER activity compared to their pristine V_2CT_x counterparts. This result suggests that controlled oxidation of vanadium carbide MXenes may serve as a strategy for improving their electrocatalytic performance rather than a drawback, opening new pathways for the use of vanadium based MXenes for electrocatalysis.[19]

Furthermore, vacancy engineering in MXenes represents a cutting-edge approach to modulating electronic structure and surface properties.[20] By introducing controlled structural defects, researchers can potentially manipulate the catalytic properties of these 2D materials. For example, Ram et al. recently explored the influence of oxygen vacancies in O-terminated $Ti_3C_2O_2$ and Mo_2CO_2 MXenes on the catalytic activity of Co single atoms adsorbed on these MXenes by computational methods. Their DOS calculations indicated that oxygen vacancies in Mo_2CO_2 lead to an increase in OER activity of the adsorbed Co, while oxygen vacancies in $Ti_3C_2O_2$ lead to a decrease. The authors explained the increased activity of the Mo_2CO_2 material by the lower potential-determining step of the conversion of •OH to •O while the decrease in the $Ti_3C_2O_2$ material was explained by the lower •O-adsorption energy E_{ads}.[20] In another recent study, Wang et al. explored the role of C vacancies coupled with strain engineering on the hydrogen evolution reaction (HER) performance of $Ti_{n+1}C_nO_2$ MXenes. The authors found that the introduction of C vacancies transformed neighboring oxygen atoms into highly active sites for $Ti_3C_2O_2$ and $Ti_4C_3O_2$, tuning their hydrogen adsorption free energy (ΔG_H*) closer to the ideal 0 eV, particularly at low hydrogen coverages while in contrast, C vacancies were found detrimental to Ti_2CO_2 due to excessively weakened hydrogen adsorption.[20]

In this work, the impact of vacancy engineering in V_2CT_x,[21] and the amount of MXene on the electrocatalytic oxygen evolution reaction performance of $Co_{0.66}Fe_{0.34}$-LDH composites in an anion exchange membrane (AEM) electrolyzer is investigated. Two distinct composite materials were synthesized and

© 2025 The Author(s). Advanced Functional Materials published by Wiley-VCH GmbH

16163028, 2026, 21, Downloaded from https://advanced.onlinelibrary.wiley.com/doi/10.1002/adfm.202503842 by Helmholtz-Zentrum Berlin Für, Wiley Online Library on [20/03/2026]. See the Terms and Conditions (https://onlinelibrary.wiley.com/terms-and-conditions) on Wiley Online Library for rules of use; OA articles are governed by the applicable Creative Commons License

16163028, 2026, 21, Downloaded from https://advanced.onlinelibrary.wiley.com/doi/10.1002/adfm.202503842 by Helmholtz-Zentrum Berlin Für, Wiley Online Library on [20/03/2026]. See the Terms and Conditions (https://onlinelibrary.wiley.com/terms-and-conditions) on Wiley Online Library for rules of use; OA articles are governed by the applicable Creative Commons License

comprehensively characterized, which were $Co_{0.66}Fe_{0.34}$-LDH supported on pristine V_2CT_x MXene and $Co_{0.66}Fe_{0.34}$-LDH anchored on V_2CT_x MXene with 10% V-vacancies. Our research aims to elucidate the fundamental mechanisms by which vacancy engineering influences the electronic and catalytic properties of MXene-supported LDH electrocatalysts. The findings in this work not only advance the understanding of MXene-supported electrocatalysts but also offer crucial design principles for developing next-generation materials for renewable energy technologies.

2. Results and Discussion

2.1. Material Synthesis and Characterization

The synthesis of $Co_{0.66}Fe_{0.34}$-LDH@V_2CT_x and $Co_{0.66}Fe_{0.34}$-LDH@$V_{1.8}CT_x$ composites was achieved through a three-step process, starting from two distinct MAX phases: V_2AlC and $V_{1.8}Cr_{0.2}AlC$ (**Figure 1a**). The first step involved selectively etching the MAX phases using concentrated hydrofluoric acid (HF). This etching process removes the Al layer (and Cr in the case of $V_{1.8}Cr_{0.2}AlC$), transforming the initial MAX phases into multilayered V_2CT_x and $V_{1.8}CT_x$ MXene structures, respectively. In the second step, these multilayered MXenes were delaminated, which promotes the formation of individual, exfoliated 2D MXene sheets. Delamination is crucial for creating an expanded surface area and enhancing the potential interaction sites for subsequent nanoparticle anchoring. The third and final step involved anchoring $Co_{0.66}Fe_{0.34}$-LDH nanoparticles onto the MXene surfaces through a modified urea-assisted thermal treatment adapted from Hao et al.[17] By varying the weight percentages of V_2CT_x and $V_{1.8}CT_x$ MXenes, a series of composite materials with targeted MXene weight ratios of 17, 33, 50, and 75 wt.% was prepared.

The resulting composite materials were labeled to reflect their targeted composition: $Co_{0.66}Fe_{0.34}$-LDH @V_2CT_x composites were denoted as CFV17, CFV33, CFV50, and CFV75, while $Co_{0.66}Fe_{0.34}$-LDH @$V_{1.8}CT_x$ composites were labeled as CFVv17, CFVv33, CFVv50, and CFVv75. To ensure comprehensive comparative analysis and to demonstrate the unique role of the MXene in the enhancement of the OER activity, reference materials were also prepared, including pure $Co_{0.66}Fe_{0.34}$ (labeled as CoFe), $Co_{0.66}Fe_{0.34}$ composites containing 33 and 75 wt.% of MAX phases V_2AlC and $V_{1.8}Cr_{0.2}AlC$ respectively (labeled as CFMAX33 and CFMAXv75), and both 33 and 75 wt.% carbon black-containing composites (labeled as CFCB33 and CFCB75).

X-ray diffraction (XRD) patterns revealed distinct structural characteristics across the synthesized materials (Figure 1c,d). The pure V_2CT_x and $V_{1.8}CT_x$ MXenes displayed characteristic reflections at (002) and (004). The absence of V_2AlC and $V_{1.8}Cr_{0.2}AlC$ specific reflections (Figure S1, Supporting Information) confirmed successful etching and delamination of the MAX phases into their respective MXene counterparts. Notably, $V_{1.8}CT_x$ exhibited a shift of the (002) reflection from 6.1° to 5.2°, indicating increased interlayer spacing, likely attributable to the presence of vacancies.[22]

The pure CoFe material showed diffraction patterns consistent with a mixture of $Co_2CO_3(OH)_2$ (PDF 00-069-0134) and $CoCuCO_3(OH)_2$ phases (PDF 00-048-0084). Given the absence of Cu in the synthesis, this can be attributed to Fe occupying the Cu sites in the crystal lattice. In the CFV series, the addition of MXene dramatically altered the crystalline structure of the CoFe phase grown (Figure 1c). All composites (except for CFV75) exhibited the formation of a distinct $Co_{0.66}Fe_{0.34}(CO_3)_{0.17}(OH)_2(H_2O)_{0.34}$-LDH phase (PDF 04-017-8816) with characteristic reflections at 11.65, 23.42, 34.08, 38.72, 46.29, 52.51, 59.18 and 60.54°, which were absent in pure CoFe. This transformation can be attributed to the hydroxyl groups on the MXene surface facilitating the adsorption of Co and Fe cations and promoting epitaxial growth of the LDH phase. A broad peak at 13° emerged in compositions from CFV17 to CFV50, intensifying with increasing MXene content, possibly indicating a decrease in LDH particle size. Notably, the characteristic MXene (002) peak disappeared in these composites, suggesting disruption of the orderly MXene stacking by ion adsorption, LDH intergrowth or oxidation of the MXene. CFV75 displayed distinct characteristics with a single prominent peak at 9.5° (potentially a shifted LDH 003 reflection, indicating an increase of interlayer spacing, and absence of other characteristic LDH peaks.

The CFVv series (Figure 1d) exhibited similar structural trends to the CFV materials, including the absence of the MXene (002) peak and formation of characteristic LDH peaks. CFVv17 uniquely appeared as a mixture of LDH and pure CoFe phases, consistent with its very low MXene content, which likely provided insufficient nucleation sites for LDH growth. With higher MXene content the peak at 13° gradually broadened reaching its maximum width in CFVv75, correlating with the decrease in particle size observed in SEM analysis of CFVv75 (Figure 1b).

Interestingly, the reference materials CFMAX33 and CFMAXv75 containing 33 wt.% V_2AlC and 75 wt.% $V_{1.8}Cr_{0.2}AlC$ MAX phases respectively also displayed the characteristic LDH reflections (Figure S1, Supporting Information). In contrast, the LDH reflections were completely absent in the reference materials CFCB33 and CFCB75 containing 33 and 75 wt.% carbon black respectively.

The morphology of the synthesized materials revealed distinct structural characteristics across different compositions. Scanning electron micrographs (SEM) of the pure V_2CT_x and $V_{1.8}CT_x$ MXenes exhibited a characteristic flake-like morphology typical of 2D nanomaterials (Figure 1b). The pristine CoFe sample demonstrated aggregates of spherical and needle-shaped particles, with an average particle size below 1 µm (Figure S2a, Supporting Information). A distinct transformation in morphology was observed in the CFV composite series compared to pristine CoFe (Figure S2b, Supporting Information). These materials exhibited well-defined platelet-shaped particles with an estimated average size of ≈1 µm. A gradual decrease in particle size was noted in the higher MXene content composites CFV50 and CFV75, suggesting that MXene content influences particle growth during synthesis.

Similar morphological trends were observed in the CFVv composites (Figure S2c, Supporting Information). CFVv17, containing the lowest MXene content in this series closely resembled pure CoFe, characterized by aggregates of spherical and needle-shaped particles – a phenomenon attributable to the very low actual MXene content. In the composites with higher MXene contents CFVv33 and 50, the morphology transitioned to

 © 2025 The Author(s). Advanced Functional Materials published by Wiley-VCH GmbH

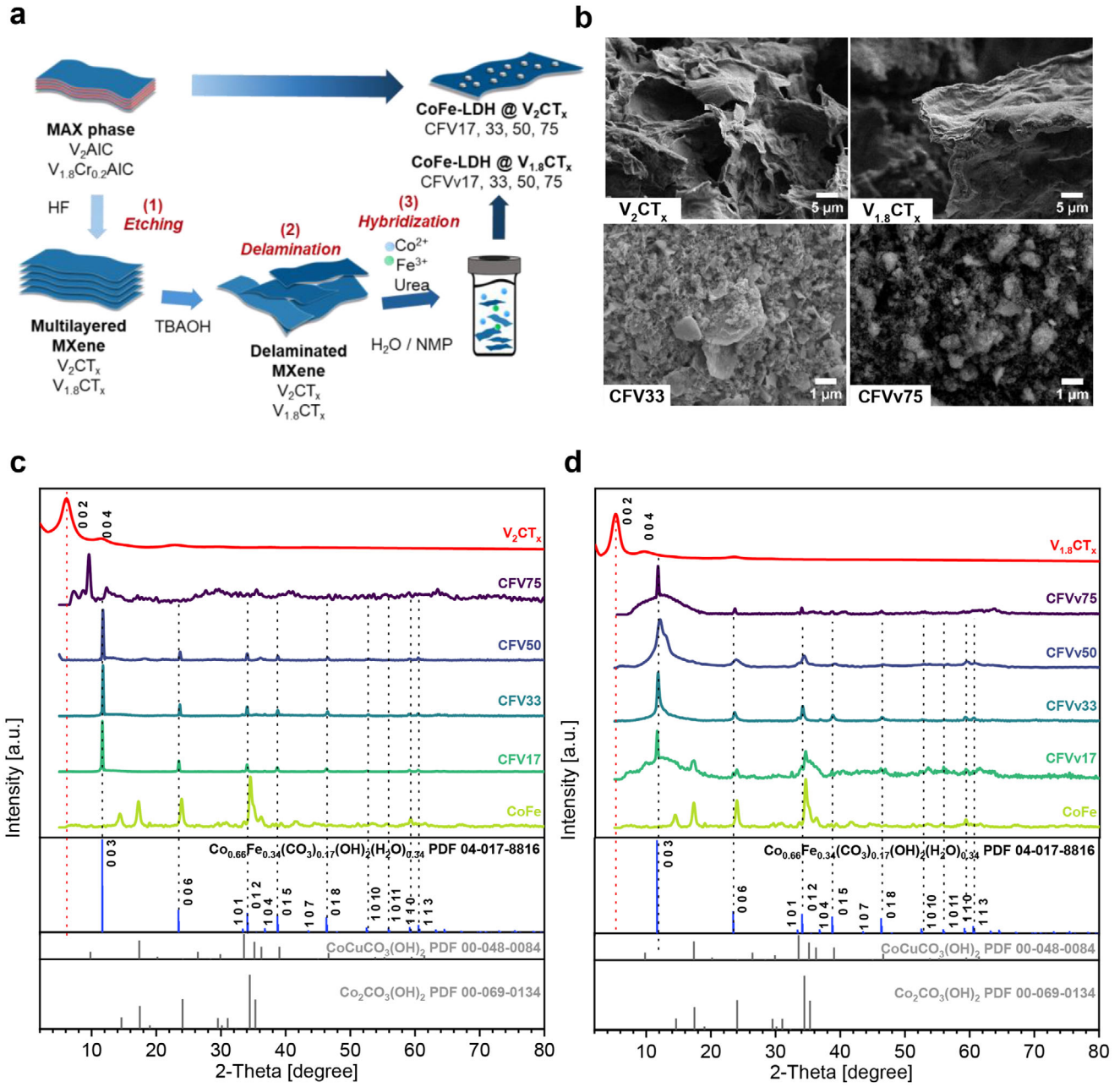

Figure 1. a) Schematic of the synthesis procedure of CoFe-LDH anchored on V_2CT_x MXenes. b) Scanning electron micrographs (SEM) of V_2CT_x -and $V_{1.8}CT_x$ MXene and CFV33 -and CFVv75 composites. c) Powder XRD patterns of CoFe, V_2CT_x and CFV composites and d) CoFe, $V_{1.8}CT_x$ and CFVv composites.

platelet-shaped particles comparable to the CFV series, with estimated particle sizes ≈1 µm. Notably, CFVv75, containing the highest MXene loading, transitioned to a morphological character distinct from other CFVv composites, featuring agglomerated spherical nanoparticles in addition to the platelet-shaped crystals.

X-ray photoelectron spectroscopy (XPS) was employed to investigate the chemical states of elements in CoFe, V_2CT_x, $V_{1.8}CT_x$, and their respective composite materials and to determine the surface composition of the Co, Fe and V elements (Figure S4a, Supporting Information). The Co 2p spectra revealed similar chemical environments across all materials containing cobalt. The peak shape of the Co 2p spectra implies that Co is predominantly present as Co(II) in both the pure CoFe and the composite materials (an increase in intensity at ≈787 eV can be attributed to the emergence of a vanadium Auger peak for higher MXene loads).[23] The shape of the Co Auger peak (Figure S4b, Supporting Information) further suggests the presence of $Co(OH)_2$.[24] Similarly, the Fe 2p spectra showed no significant changes in the chemical state of iron between the pure CoFe and the composite materials, indicating that the interaction with MXene

© 2025 The Author(s). Advanced Functional Materials published by Wiley-VCH GmbH

16163028, 2026, 21, Downloaded from https://advanced.onlinelibrary.wiley.com/doi/10.1002/adfm.202503842 by Helmholtz-Zentrum Berlin Für, Wiley Online Library on [20/03/2026]. See the Terms and Conditions (https://onlinelibrary.wiley.com/terms-and-conditions) on Wiley Online Library for rules of use; OA articles are governed by the applicable Creative Commons License

supports did also not substantially alter the electronic structure of the Fe species. Judging from the peak shape and the small satellite at ≈719 eV iron is most likely present as Fe(III). However, due to the weak signal, the presence/transformation to a mixture of Fe(II)/Fe(III) cannot be ruled out.[25] Analysis of the V 2p region indicated that vanadium existed primarily as V(V) in both CFV and CFVv composite materials, which suggest complete oxidation of the MXenes at the catalyst surface. This oxidation state remained consistent across both V_2CT_x and $V_{1.8}CT_x$ -based composites, suggesting similar surface chemistry despite the structural differences between the two MXene supports. The surface composition of Co, Fe and V was determined from the Co 2p, Fe 2p and V 2p core levels and the Co:Fe and V:CoFe atomic ratios were determined (Figure S4d, Supporting Information).

Inductively coupled plasma optical emission spectroscopy (ICP-OES) was conducted to determine the atomic weight ratios of Co, Fe, V, and Cr in the pure materials (CoFe, V_2CT_x and $V_{1.8}CT_x$ MXenes) and their respective composite materials (CFV and CFVv series) (Figure S3, Supporting Information). The V content in both pure MXenes was significantly lower than theoretically calculated values, with V_2CT_x showing 22% (vs calculated 69%) and $V_{1.8}CT_x$ showing 23% (vs calculated 62%). This discrepancy might be attributed to an overestimation of the dried MXene weight, potentially due to intercalated ions and water molecules between the MXene layers. $V_{1.8}CT_x$ still contained 2.4% of the initial 10% of Cr in relation to V, indicating that around ¾ of Cr was removed during etching. This could also be observed in XPS (not shown). Analysis of the pure CoFe material revealed a higher Co:Fe ratio than expected (3.4 vs theoretical 2.0), indicating a lower precipitation rate of the Fe precursor compared to Co during synthesis, with excess Fe likely being removed during the washing process. The CFV series showed a general trend of increasing Co:Fe ratio with higher MXene loading, with CFV50 being a notable exception, displaying the lowest Co:Fe ratio among the CFV materials. The V content in these materials closely matched theoretical calculations, except for CFV75, where the observed content (39%) was notably lower than the expected (52%). This deviation might result from incomplete coverage of excess MXene by $Co_{0.66}Fe_{0.34}$-LDH during synthesis, leading to material loss during washing. The CFVv series exhibited similar trends, albeit less pronounced, with the Co:Fe ratio gradually increasing with higher MXene loading. However, these materials showed consistently lower V content compared to theoretical values. This observation might be explained by a more significant overestimation of MXene weight during preparation, potentially due to increased intercalation of ions and water within the wider interlayer spaces characteristic of $V_{1.8}CT_x$ compared to V_2CT_x. The CFVv materials also contained Cr in proportion to the V content.

To gain insights into potential surface segregation effects, the elemental ratios obtained from ICP-OES (bulk composition, Figure S4c, Supporting Information) and XPS (surface composition, Figure S4d, Supporting Information) measurements were compared. The Co:Fe ratio consistently showed higher values in XPS measurements compared to ICP-OES for all materials except CFVv17, suggesting a general tendency for Co enrichment at the material surfaces. This can be explained by the embedment of Fe into a $Co(OH)_2$ lattice in as is suggested for cobalt-iron hydroxides.[26] In contrast, the V:CoFe ratios showed good agreement between bulk and surface measurements across all materials, indicating a more uniform distribution of vanadium throughout the composite structures.

N_2 adsorption–desorption isotherms and pore size distribution of $V_{1.8}CT_x$ and V_2CT_x are shown in Figure S5 (Supporting Information). The presence of a Type IV hysteresis loop suggests a contribution from mesoporous structures, likely arising from interlayer spacing. The specific surface areas were determined using the Brunauer-Emmett-Teller (BET) method with a multipoint analysis. The $V_{1.8}CT_x$ exhibited a surface area of 8.1 $m^2\ g^{-1}$, while V_2CT_x measured 5.6 $m^2\ g^{-1}$. This aligned well with the expectation that the introduction of vacancies to V_2CT_x would increase the specific surface area of the MXene. Moreover, the pore size distribution was analyzed using the Barrett-Joyner-Halenda (BJH) model. Both $V_{1.8}CT_x$ and V_2CT_x exhibited pore sizes ranging from 3 to 10 nm, suggesting that interlayer spacing is the dominant structural feature within the pore structure.

Zeta potential measurements of the synthesized V_2CT_x, $V_{1.8}CT_x$, pure CoFe and CFV and CFVv composites were conducted to provide insights into surface charge modifications and particle interactions (Figure S6, Supporting Information). Bare V_2CT_x and $V_{1.8}CT_x$ exhibited negative zeta potentials of −8.59 mV and −5.03 mV respectively, indicating negatively charged surfaces due to surface terminations such as –O, –OH, and –F. The relatively low absolute potential values suggest that the surface of both MXenes is predominantly terminated by F atoms. The pure CoFe sample displayed a positive zeta potential of 5.63 mV, confirming the presence of positively charged hydroxyl groups or metal cations. In the composite materials, a shift in zeta potential toward more neutral values was observed, reflecting charge compensation and surface interactions. The V_2CT_x-based composites exhibited zeta potentials between −4 and −3 mV across all samples, showing that even at the highest MXene loading (CFV75) the charge compensation from surface coverage by CoFe-LDH was comparable to the lowest loading (CFV17).

A similar charge compensation was observed for the $V_{1.8}CT_x$ composites, with the less negative values of the CFVv materials reflecting the lower zeta potential value of the pure $V_{1.8}CT_x$ compared to V_2CT_x. Notably CFVv17 demonstrated a more positive potential (7.82 mV) than even pure CoFe, which could be explained by its very low actual MXene content and its partial CoFe-LDH content which is exhibits a more positive zeta potential than the cobalt-iron oxides in the pure CoFe sample. Furthermore, in contrast to the CFV materials, a minimum zeta potential was reached by CFVv50 (−4.23 mV) while CFVv75 had a more neutral potential (−1.8 mV) despite its higher MXene content. This behavior could be explained by the decrease in CoFe-LDH particle size from CFVv50 to CFVv75, resulting in a higher charge compensation from increased surface interaction. In summary, these results suggest that LDH decoration effectively modifies the MXene surface charge, with the extent of neutralization depending on the MXene composition and CoFe-LDH loading.

2.2. Electrochemical Evaluation

To elucidate the redox processes and electronic interactions between the components the CFV and CFVv composites and the

© 2025 The Author(s). Advanced Functional Materials published by Wiley-VCH GmbH

16163028, 2026, 21, Downloaded from https://advanced.onlinelibrary.wiley.com/doi/10.1002/adfm.202503842 by Helmholtz-Zentrum Berlin Für, Wiley Online Library on [20/03/2026]. See the Terms and Conditions (https://onlinelibrary.wiley.com/terms-and-conditions) on Wiley Online Library for rules of use; OA articles are governed by the applicable Creative Commons License

16163028, 2026, 21, Downloaded from https://advanced.onlinelibrary.wiley.com/doi/10.1002/adfm.202503842 by Helmholtz-Zentrum Berlin Für, Wiley Online Library on [20/03/2026]. See the Terms and Conditions (https://onlinelibrary.wiley.com/terms-and-conditions) on Wiley Online Library for rules of use; OA articles are governed by the applicable Creative Commons License

pure CoFe reference material were investigated using cyclic voltammetry (Figure S7, Supporting Information).

Pure CoFe exhibited a semi-reversible redox peak centered at 1.2 V, attributable to Co^{2+}/Co^{3+} transitions. This peak showed decreased intensity and shifted to lower potentials after the first cycle, suggesting surface restructuring during initial polarization. An additional redox feature was observed at 1.45 V, corresponding to Fe^{3+}/Fe^{4+} redox transitions. In the CFV (CoFe-LDH@V_2CT_x) composites significant changes in the voltammetric response compared to pure CoFe were observed. The first cycle revealed an intense, broad irreversible oxidation peak in the range of 1.4–1.5 V, likely arising from overlapping Co^{2+}/Co^{3+} and V^{4+}/V^{5+} oxidation processes. A clear composition-dependent trend was identified in the reversible redox peak, which gradually shifted from 1.3 to 1.2 V with increasing V_2CT_x content (from CFV17 to CFV75). Notably, CFV50 deviated from this trend, displaying the reversible feature at 1.45 V, which may indicate an optimal compositional ratio for unique interfacial interactions. All CFV materials demonstrated significantly enhanced capacitive currents between 1.1 and 1.5 V, characteristic of the pseudocapacitive behavior contributed by the V_2CT_x MXene component. The CFVv (CoFe-LDH@$V_{1.8}CT_x$) composites, presented similar voltammetric profiles to their CFV counterparts but with notable differences. The irreversible oxidation peak in the first cycle appeared less intense, consistent with the lower vanadium content in these materials. Interestingly, CFVv75, despite containing the highest proportion of vanadium among the CFVv materials, exhibited the least intense irreversible peak. This suggests MXene stabilization through enhanced surface coverage by CoFe-LDH at this compositional ratio. In contrast to the CFV materials, the CFVv series lacked the characteristic reversible redox peak at 1.2-1.3 V, indicating fundamentally different electronic properties and interactions between CoFe-LDH and $V_{1.8}CT_x$ compared to V_2CT_x.

The OER activity of the synthesized materials was evaluated through linear sweep voltammetry (LSV). The typical LSV curves of the pure CoFe, V-MXenes, and the composite materials are presented in **Figure 2**a,b, while the corresponding average overpotentials η_{10} required to achieve a current density of 10 mA cm^{-2} are depicted in Figure 2c,f. From the LSV curves, all composite materials demonstrated enhanced OER activity compared to pure CoFe and pristine MXenes, as evidenced by lower overpotentials at 10 mA cm^{-2}. Importantly, these composites also outperformed their respective reference materials (CFMAX and CFCB). The superior activity of CoFe@MXene composites over CoFe@MAX-phase composites is particularly significant, as XRD analysis confirmed the presence of identical CoFe-LDH phases in both materials (Figure 1; Figure S1, Supporting Information). This performance difference emphasizes the critical role of MXene-CoFe interactions in enhancing catalytic activity, suggesting a synergistic effect that extends beyond simple physical mixing of the components.

In the CoFe@V_2CT_x (CFV) series, relatively consistent overpotentials were observed across different MXene loadings, with the lowest overpotential of 317 mV at 10 mA cm^{-2} being achieved by CFV33. The overpotentials for this series were determined as CFV33 (317 mV) < CFV17 (320 mV) < CFV75 (323 mV) < CFV50 (343 mV). The slight deviation in CFV50's performance can be attributed to its unique compositional characteristics previously identified in the structural analyses. A clear trend of decreasing overpotentials with increasing MXene content was observed in the CoFe@V_2CT_x (CFVv) series. The performance was found to improve systematically from CFVv17 (360 mV) to CFVv75 (304 mV), with CFVv75 achieving not only the lowest overpotential within its series but also the best overall performance among all tested materials. This trend suggests that the vacancy-engineered $V_{1.8}CT_x$ MXene support significantly enhances catalytic activity of the resulting composites, particularly at higher MXene loadings.

To elucidate the relationship between elemental composition and catalytic performance, the correlation between overpotentials at 10 mA cm^{-2} and atomic weight ratios as determined by ICP-OES (Figures S3 and S4c, Supporting Information), was analyzed focusing on the Co:Fe and V:CoFe ratio across the synthesized materials (Figure 2). The Co:Fe ratio demonstrated different optimal values for each series of composites. In the CFV materials (Figure 2d), activity increased with higher Co content until reaching the optimal overpotential at a Co:Fe ratio of 2.75 in CFV33, beyond which performance declined. The CFVv series (Figure 2g), displayed a similar trend of enhanced activity with increasing Co content, even though variations in the Co:Fe ratios compared to the CFV series were less pronounced. Notably, the CFVv materials achieved optimal performance at a significantly lower Co:Fe ratio of 1.65. This difference suggests that the presence of vacancies in the $V_{1.8}CT_x$ support influenced the optimal Co:Fe composition required for maximum catalytic activity.

Interestingly, both CFV and CFVv series converged to optimal performance at a similar V:CoFe ratio of ≈0.8 (Figure 2e,h), indicating that despite their structural differences, both MXene supports require similar relative vanadium content to maximally enhance catalytic activity. This convergence points to a fundamental relationship between the MXene support's vanadium content and the composite's electrocatalytic performance, regardless of the presence of vacancies.

To gain deeper insights into the charge transfer kinetics, galvanostatic electrochemical impedance spectroscopy (EIS) at 10 mA cm^{-2} was conducted. The averaged Nyquist plots for CFV and CFVv series are presented in **Figure 3**a,b, respectively, with the charge transfer resistance (R_{ct}) evaluated from the diameter of the semicircles. In the CFV series, R_{ct} values correlated well with OER activity, following the trend CFV17 ≈ CFV33 < CFV75 < CFV50. Notably, CFV50 was the only composite showing higher R_{ct} than pure CoFe. The CFVv series demonstrated a more complex relationship between R_{ct} and catalytic activity. While CFVv50 exhibited the lowest R_{ct} among all materials despite higher overpotential than CFVv75, CFVv17 showed marginally lower R_{ct} than pure CoFe, and CFVv33 unexpectedly displayed higher R_{ct} despite both materials demonstrating superior OER activity compared to pure CoFe.

Tafel analysis was performed to elucidate the reaction kinetics and mechanistic aspects of the OER process. CoFe exhibited a Tafel slope of 55.6 mV dec^{-1} indicating that the second step of the OER mechanism, the formation of the O^* intermediate ($OH^* + OH^-_{(aq)} \rightarrow O^* + H_2O_{(aq)} + e^-$), is the rate determining step as suggested by Fan et al.[27] The Tafel plots (Figure 3c,d) revealed a general trend of decreasing values with increasing MXene content up to ≈30% real MXene weight percentage. The CFV catalysts revealed Tafel slopes

© 2025 The Author(s). Advanced Functional Materials published by Wiley-VCH GmbH

16163028, 2026, 21, Downloaded from https://advanced.onlinelibrary.wiley.com/doi/10.1002/adfm.202503842 by Helmholtz-Zentrum Berlin Für, Wiley Online Library on [20/03/2026]. See the Terms and Conditions (https://onlinelibrary.wiley.com/terms-and-conditions) on Wiley Online Library for rules of use; OA articles are governed by the applicable Creative Commons License

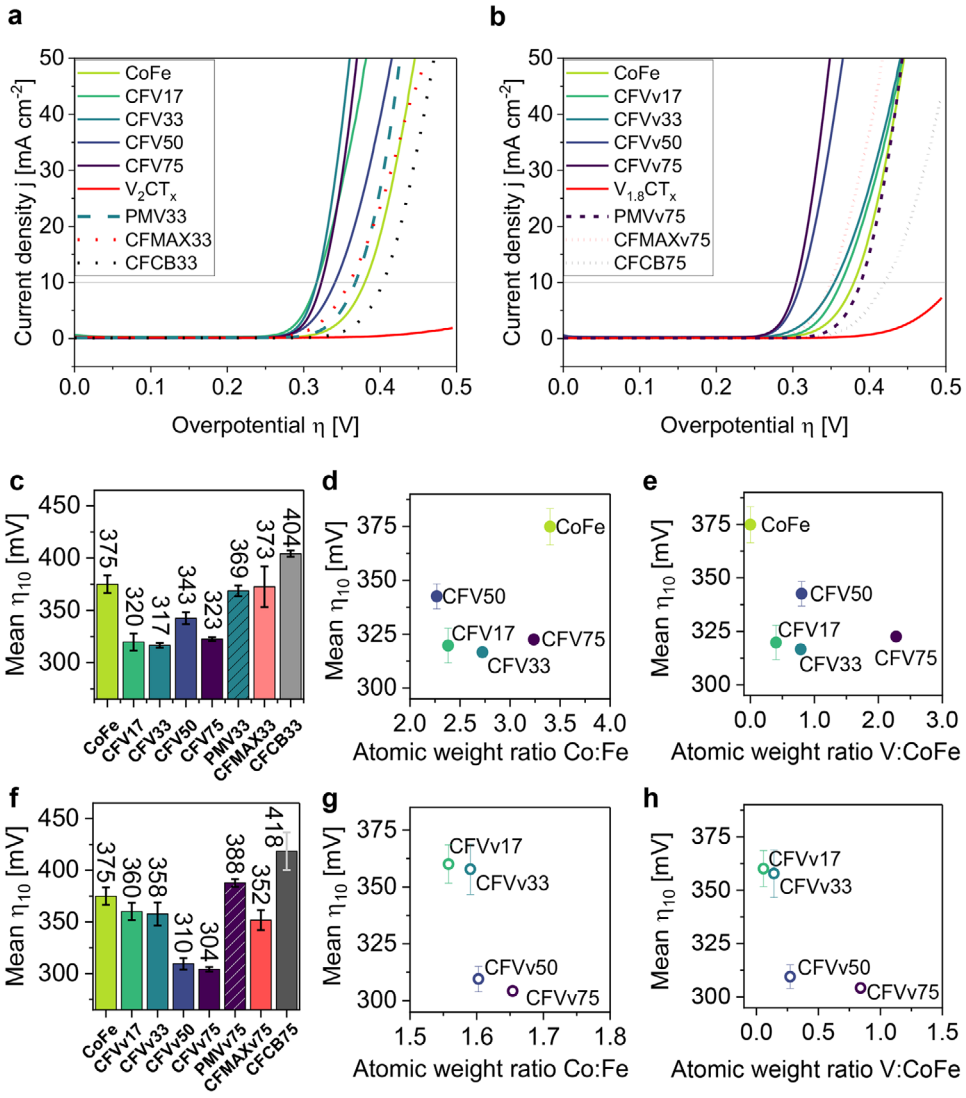

Figure 2. a–b) Linear sweep voltammograms of CoFe, pure MXenes V_2CT_x and $V_{1.8}CT_x$, composite materials CFV and CFVv, and reference materials PMV, PMVv, CFMAX, CFMAXv and CFCB. The current is normalized by the geometric area of the working electrode (WE). c) Mean OER overpotentials at 10 mA cm^{-2} (η_{10}), d) η_{10} plotted against the Co:Fe atomic weight ratio and e) η_{10} plotted against the V:CoFe atomic weight ratio determined by ICP-OES of CoFe and CFV composites. f) Mean OER overpotentials at 10 mA cm^{-2} (η_{10}), g) η_{10} plotted against the Co:Fe atomic weight ratio and h) η_{10} plotted against the V:CoFe atomic weight ratio determined by ICP-OES of CFVv composites.

ranging from 34.8 to 47.6 mV dec^{-1}. Notably, CFV33, CFV75 CFVv50 and CFVv75 demonstrated Tafel slopes below 40 mV dec^{-1}, suggesting the third step, the formation of OOH* ($O^* + OH^-_{(aq)} \rightarrow OOH^* + e^-$) or the fourth step, the formation of O_2 ($OOH^* + OH^-_{(aq)} \rightarrow O_2 + H_2O_{(aq)} + e^-$) as rate determining step.[5,28] These trends aligned with OER activity measurements, with the best-performing composites CFV33 and CFVv75 exhibiting the lowest Tafel slopes. CFV50 and CFVv33 emerged as outliers from this correlation between MXene loading and OER activity.

To better understand the relationship between surface properties and catalytic performance, the electrochemically active surface area (ECSA) of the pure $V_{1.8}CT_x$ and V_2CT_x MXenes, pure CoFe and CFV and CFVv composites was determined using the electrical double-layer capacitance C_{dl} performing cyclic voltammetry at varying scan rates in the non-faradaic potential region (Figure S9, Supporting Information).

Interestingly, the pure CoFe reference material demonstrated a higher ECSA than all composite materials, presenting an apparent contradiction given the superior OER activity observed for the hybrid catalysts. This suggests that the enhanced electrocatalytic performance of the composite materials cannot be attributed solely to increased surface area but rather indicates the presence of more efficient active sites, improved electron transfer properties, and beneficial electronic interactions between the CoFe-LDH and MXene components.

For the CFV series containing V_2CT_x the ECSA values followed a non-monotonic trend with respect to MXene content, reaching maximum values at intermediate compositions (36 cm^2 g^{-1} for both CFV33 and CFV50) before decreasing at the highest

© 2025 The Author(s). Advanced Functional Materials published by Wiley-VCH GmbH

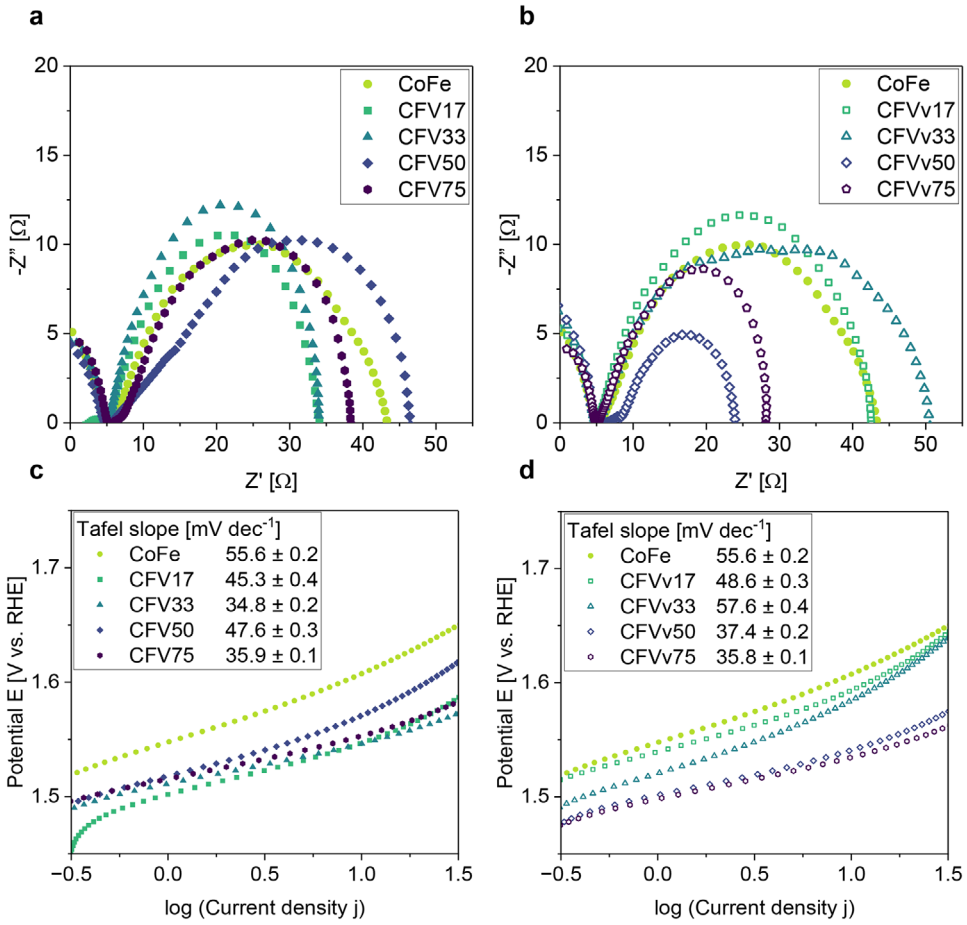

Figure 3. Nyquist plots of a) CoFe and CFV composites and b) CoFe and CFVv composites, measured at 10 mA cm^{-2} current density. Tafel plots of c) CoFe and CFV composites and d) CoFe and CFVv composites.

MXene loading (26 cm^2 g^{-1} for CFV75). This trend suggests that initial increases in MXene content create optimal interfaces with CoFe-LDH, while excessive MXene loadings may lead to partial agglomeration or stacking of MXene sheets, thereby reducing the accessible electrochemical surface area.

Similarly, the CFVv series with $V_{1.8}CT_x$ exhibited a comparable trend, with ECSA values peaking at medium MXene loading (31 cm^2/g for CFVv50) and declining sharply at the highest loading (15 cm^2/g for CFVv75). Notably, the CFVv materials consistently displayed lower ECSA values compared to their CFV counterparts despite the higher intrinsic ECSA of pure $V_{1.8}CT_x$ relative to V_2CT_x. This unexpected result, particularly when considered alongside the superior OER performance of CFVv materials, suggests either significantly higher turnover frequencies (TOFs) at the active sites in these composites or limitations in the C_{dl} method for accurately quantifying the electrochemically active surface area in these porous nanostructured systems. Furthermore, analysis of the pure MXene components revealed that $V_{1.8}CT_x$ exhibited a notably higher ECSA (32 cm^2 g^{-1}) compared to V_2CT_x (23 cm^2 g^{-1}) (Figure S9f, Supporting Information), confirming the BET surface area measurements (Figure S6, Supporting Information). This observation confirms that the introduction of vanadium vacancies in the MXene structure creates additional accessible surface sites, likely enhancing electrolyte penetration and ion accessibility.

Long-term stability tests were conducted on the most promising catalysts, CFV33 and CFVv75, using chronopotentiometry at a constant current density of 100 mA cm^{-2} over 12 h (Figure S10a, Supporting Information). Both materials maintained superior performance compared to the CoFe reference, operating at lower overpotentials (CFV33: 435 mV, CFVv75: 440 mV vs CoFe: 505 mV) throughout the testing period. The materials showed excellent stability with only minimal performance degradation, evidenced by slight overpotential increases of 1.4 mV h^{-1} and 1.0 mV h^{-1} for CFV33 and CFVv75, respectively.

To investigate potential catalyst degradation during OER, ICP-OES analysis of the electrolyte solution was carried out following chronopotentiometry measurements (Figure S10b, Supporting Information). The analysis revealed minimal leaching of Co and Fe (<0.1%) across all samples, indicating good stability of the catalytically active species. However, both composite materials exhibited substantial leaching of vanadium into the electrolyte, with CFV33 and CFVv75 losing ≈40% and 62% of their initial V content, respectively.

XPS analysis comparing the catalysts before and after OER provided further insights into the chemical state evolution of

© 2025 The Author(s). Advanced Functional Materials published by Wiley-VCH GmbH

16163028, 2026, 21, Downloaded from https://advanced.onlinelibrary.wiley.com/doi/10.1002/adfm.202503842 by Helmholtz-Zentrum Berlin Für, Wiley Online Library on [20/03/2026]. See the Terms and Conditions (https://onlinelibrary.wiley.com/terms-and-conditions) on Wiley Online Library for rules of use; OA articles are governed by the applicable Creative Commons License

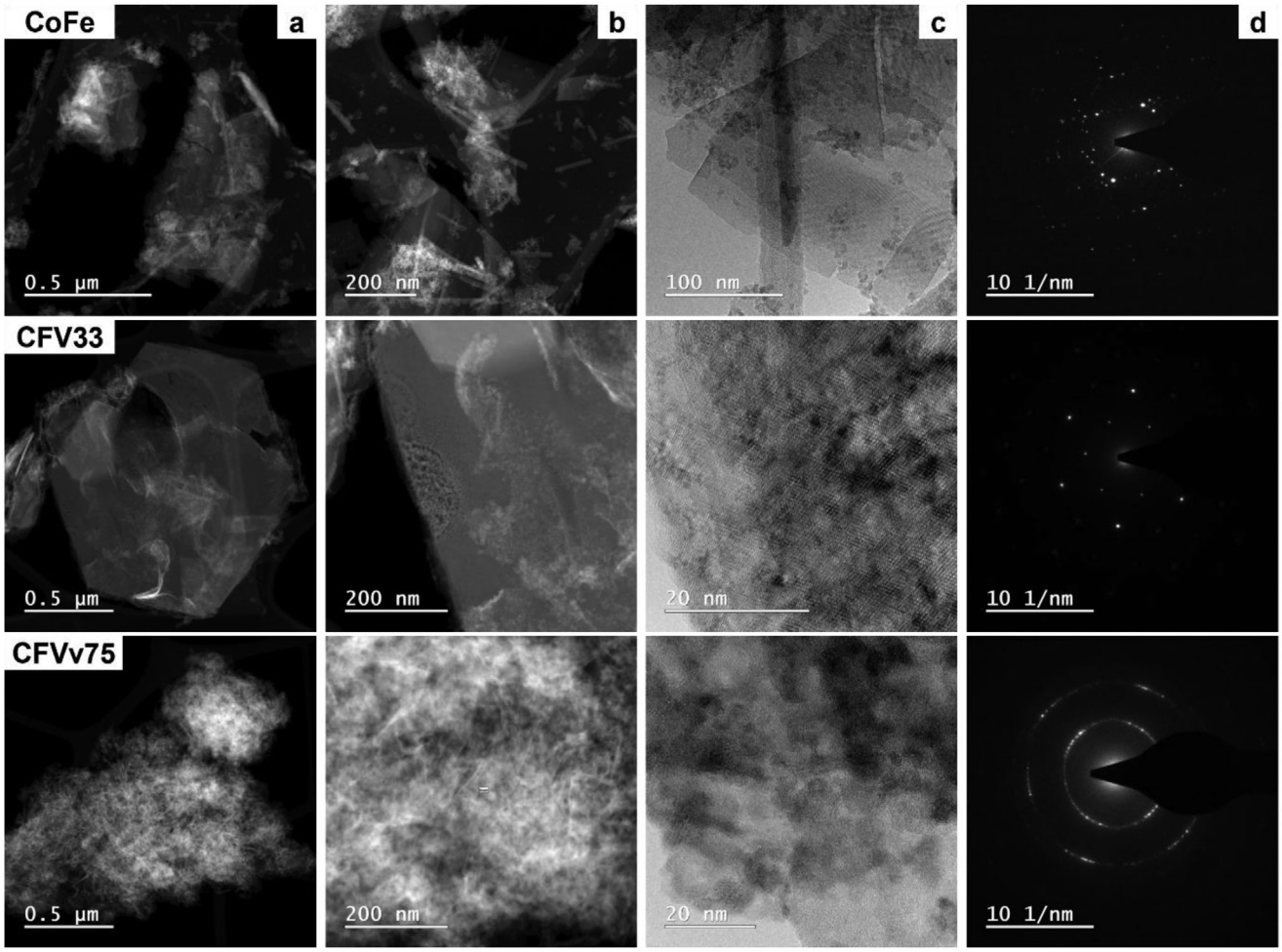

Figure 4. TEM images of as prepared CoFe, CFV33 and CFVv75 samples. a,b) HAADF-STEM, c) HR-TEM and d) SAED images.

the materials (Figure S10c, Supporting Information). The Co 2p spectra showed that cobalt existed predominantly as Co(II) in the materials before OER, transforming to Co(II/III) states after OER in all three catalysts.[25,29] The Fe 2p signal exhibited interesting behavior, increasing in intensity for the composite materials while showing a slight decrease in pure CoFe. Post-mortem analysis indicated that iron predominantly preserved its Fe(III) oxidation state. Notably, the V 2p spectra of both composites revealed that vanadium was initially present as V(V), but the signal completely disappeared after OER, corroborating the ICP-OES findings of significant V leaching. This observation suggests a substantial chemical degradation of the MXene support during the catalytic process, which may contribute to the enhanced catalytic performance observed in the composite materials.

Detailed structural characterization was performed using transmission electron microscopy (TEM) on the pure CoFe sample, as well as the composites CFV33, and CFVv75 (**Figure 4**) which were selected based on their comparable V content as determined by ICP analysis as well as their outstanding OER performance as demonstrated in Figure 2.

The High-Angle Annular Dark-Field (HAADF) Scanning Transmission Electron Microscopy (STEM) and High-Resolution Transmission Electron Microscopy (HRTEM) observations confirmed and expanded upon the morphological features previously identified by SEM (Figure S2, Supporting Information). Pure CoFe exhibited a heterogeneous structure composed of tabular and rod-like microcrystals alongside spherical nanoparticles, consistent with the mixed-phase composition suggested by XRD analysis. Selected area electron diffraction (SAED) patterns of pure CoFe showed numerous diffraction spots of varying intensities with complex symmetry, suggesting grains of different sizes and further confirming its multi-phase nature.

CFV33 revealed well-defined layered hexagonal platelets with an average size of 1 µm, supporting the formation of the $Co_{0.66}Fe_{0.34}(CO_3)_{0.17}(OH)_2(H_2O)_{0.34}$-LDH phase identified by XRD. The SAED pattern displayed sharp diffraction spots arranged in two concentric circles, representing two major diffraction planes from the crystal (likely (003) and (006)). The six sharp spots per circle indicate a highly ordered hexagonal crystal structure characteristic of LDH materials.[5]

In contrast, CFVv75 consisted of aggregated, few-nm nanoparticles exhibiting a layered structure. Its SAED pattern showed two continuous concentric rings instead of discrete spots, attesting the lack of a preferred orientation, indicating a poly- or

© 2025 The Author(s). Advanced Functional Materials published by Wiley-VCH GmbH

16163028, 2026, 21, Downloaded from https://advanced.onlinelibrary.wiley.com/doi/10.1002/adfm.202503842 by Helmholtz-Zentrum Berlin Für, Wiley Online Library on [20/03/2026]. See the Terms and Conditions (https://onlinelibrary.wiley.com/terms-and-conditions) on Wiley Online Library for rules of use; OA articles are governed by the applicable Creative Commons License

16163028, 2026, 21, Downloaded from https://advanced.onlinelibrary.wiley.com/doi/10.1002/adfm.202503842 by Helmholtz-Zentrum Berlin Für, Wiley Online Library on [20/03/2026]. See the Terms and Conditions (https://onlinelibrary.wiley.com/terms-and-conditions) on Wiley Online Library for rules of use; OA articles are governed by the applicable Creative Commons License

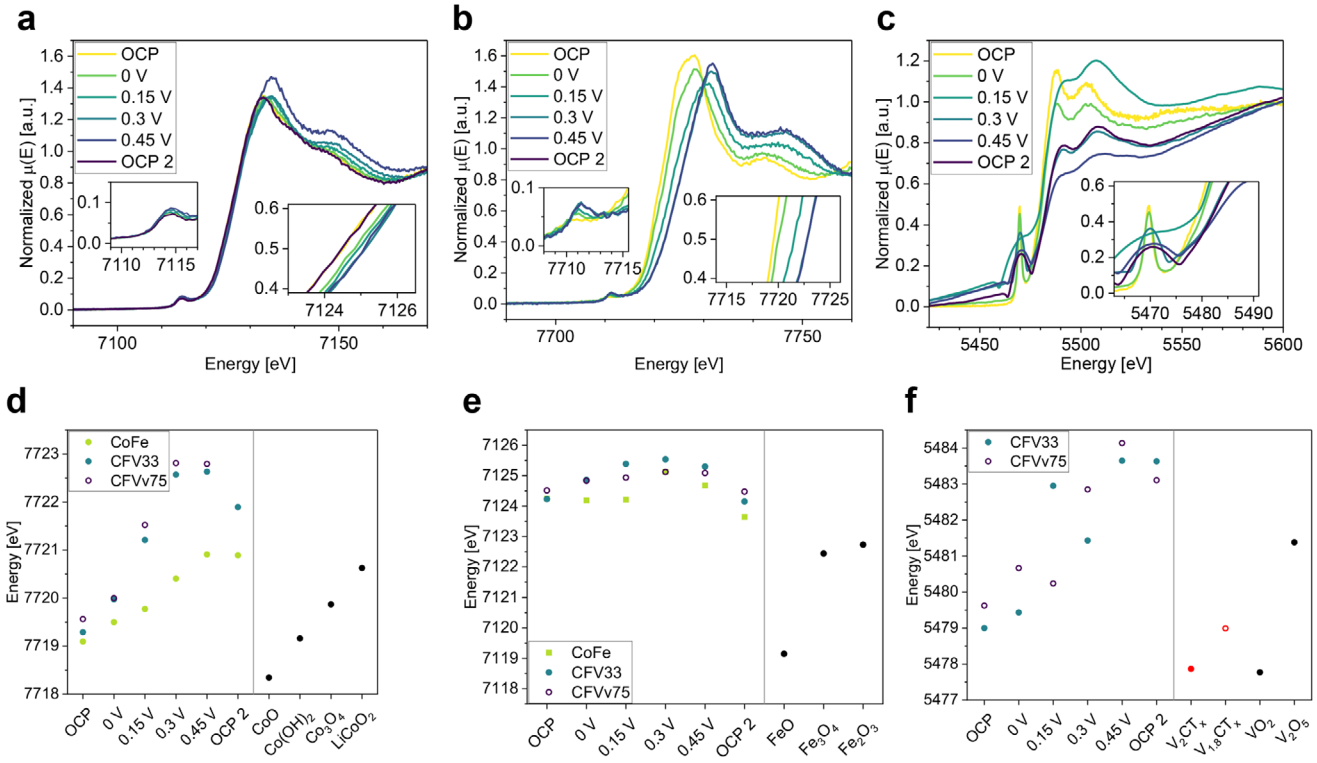

Figure 5. a) XANES spectra showing the Co, b) Fe, -and c) V K-edge and pre-edge of CFVv75 at OCP and various applied OER overpotentials η. d) Co edge energies of CoFe, CFV33 and CFVv75 plotted against the applied overpotential and ex-situ energies of CoO, $Co(OH)_2$, Co_3O_4, $LiCoO_2$ references. e) Fe edge energies of CoFe, CFV33 and CFVv75 plotted against the applied overpotential and ex-situ energies of FeO, Fe_2O_3, Fe_3O_4 references. f) V edge energies of CFV33 and CFVv75 plotted against the applied overpotential and ex-situ energies of V_2CT_x, $V_{1.8}CT_x$, and VO_2 and V_2O_5 references.

nanocrystalline material. The slightly larger radii of the circles compared to CFV33 suggest a similar but more condensed crystal structure.

These observations provide strong evidence that the incorporation of different MXene supports fundamentally alters the morphology and crystalline structure of the CoFe-based materials. The morphological difference between CFV33 and CFVv75 could contribute to the superior OER activity of CFVv75 shown in Figure 2. Indeed, it has been shown that amorphous and nanocrystalline catalysts show better catalytic performance than their crystalline counterparts which can be explained by features such as their larger specific surface area, flexible electronic structure, and deep structure reconstruction during the electrocatalytic process.[30] In conclusion, the structural analysis presented here highlights the critical importance of designing nanocrystalline catalysts for improved electrochemical applications.

2.3. X-Ray Absorption Spectroscopy Under Operating Conditions

To gain deeper insight into the electronic structure evolution during OER, synchrotron-based in situ X-ray absorption spectroscopy (XAS) was conducted on CoFe and the composite materials. The Co, Fe, and V edges were examined to determine oxidation states before, during, and after OER, revealing changes with applied potential.

Analysis of the Co K-edge XANES spectra (**Figure** 5d) revealed significant electronic and structural transformations during OER catalysis. At open circuit potential (OCP), all materials exhibited edge energies (7719.1–7719.6 eV) close to the $Co(OH)_2$ reference, confirming a predominant +2 oxidation state, consistent with XPS results. Interestingly, the composite materials CFV33 and CFVv75 displayed slightly higher initial edge energies (7719.3 and 7719.6 eV) compared to pure CoFe (7719.1 eV), suggesting subtle electronic structure modifications induced by the presence of MXene components.

As the potential increased to η = 0.45 V, a pronounced edge shift was observed, with CFV33 and CFVv75 demonstrating significantly larger energy shifts (ΔE_{Co} of 3.3 and 3.2 eV) relative to pure CoFe (ΔE_{Co} of 1.8 eV). The final edge energies reached by CFV33 (7722.6 eV) and CFVv75 (7722.8 eV) substantially exceeded that of the $LiCoO_2$ reference (Co^{3+}), providing clear spectroscopic evidence for the formation of Co(IV) species. The progressive shift of the absorption edge to higher energies with increasing potential reflects the stepwise oxidation of $Co^{2+} \rightarrow Co^{3+} \rightarrow Co^{4+}$, with the latter serving as a crucial intermediate in the OER mechanism.

Pre-edge features in the Co K-edge XANES spectra provide valuable insights into the local coordination geometry of Co centers (Figure 5a; Figure S11a,c, Supporting Information). At OCP, all samples showed weak pre-edge intensity typical for octahedrally coordinated Co(II) species. Upon oxidation during OER, the pre-edge intensity increased significantly for the composite

© 2025 The Author(s). Advanced Functional Materials published by Wiley-VCH GmbH

materials CFV33 and CFVv75, with a clear trend of increasing intensity with applied potential. This enhancement indicates progressive distortion of the Co-O_6 octahedra and possible changes in the hybridization between Co 3d and O 2p orbitals. In stark contrast, the pure CoFe sample showed different behavior – initially exhibiting a slight increase in pre-edge intensity at intermediate potentials but then decreasing back to nearly the initial intensity level at the highest applied potential (0.45 V). Significantly, when returning to OCP after OER, the white line positions for all three materials remained nearly identical to those at 0.45 V, clearly demonstrating that the electronic structure changes in Co centers are irreversible across all samples. This irreversibility suggests permanent modification of the Co coordination environment during OER, likely due to structural reconstruction of the catalyst surface. The persistent elevated edge energies after OER indicate that the catalytically relevant high-valent Co species remain stabilized even after removing the applied potential, which may contribute to the sustained catalytic activity observed in these materials.

The FT-EXAFS analysis provides further insights into the structural transformations of the catalysts during OER. For pure CoFe at OCP, two overlapping contributions at 1.33 Å and 1.76 Å were observed, corresponding to Co—O bonds in the first coordination shell (Figure S12a, Supporting Information). As the potential increased to 0.3 V, these features merged into a single peak at ≈1.5 Å, indicating a more uniform Co—O bonding environment. With further potential increase to 0.45 V and beyond, significant restructuring occurred, evidenced by the development of a broader peak at 1.4 Å and the emergence of a new feature at 2.55 Å, which can be attributed to Co-Co scattering in the second coordination shell. At the highest potential (0.75 V), the peak at 2.55 Å intensified and showed an additional shoulder at 2.27 Å, suggesting the formation of new Co-Co interactions characteristic of edge-sharing CoO_6 octahedra in the active catalyst state. Interestingly, upon returning to OCP, the first-shell Co-O peak at 1.33 Å showed the highest intensity observed in the series, with retention of the Co-Co features developed at high potential, confirming the irreversible nature of the local structure changes.

The composite materials exhibited distinctly different coordination evolution patterns. CFV33 initially showed two sets of overlapping peaks at OCP (1.14/1.7 Å and 2.61/2.95 Å), corresponding to the Co-O first shell and Co-Co/Co-Fe second shell, respectively (Figure S12c, Supporting Information). With increasing potential, these evolved toward more defined single peaks at 1.36-1.46 Å (first shell) and 2.56-2.61 Å (second shell), with a characteristic shoulder at ≈2.2 Å emerging at potentials of 0.45 V and above. This shoulder likely represents the formation of shorter Co—M (M = Co, Fe, V) bonds that facilitate electron transfer during catalysis. The CFVv75 material followed a similar trend but demonstrated an even more pronounced transformation, with rapid coalescence of the first-shell peaks into a single, intense feature at 1.47 Å even at moderate potentials (0.3 V, Figure S12e, Supporting Information). These findings align with recent studies from Zhao et al., who demonstrated that tetrahedral Co(II) centers undergo dynamic transformation into highly active Co(IV) intermediates during OER catalysis.[31] Their work showed that such transformations can be facilitated by partial Fe incorporation – similar to our observation that the presence of MXene components with V enhances the structural rearrangement and stabilization of catalytically active Co(IV) species. Additionally, the bond contractions we observe in the Co-O shell upon oxidation (from ≈1.7 Å to 1.4 Å) are consistent with the formation of the high-valent Co(IV)-oxo species proposed as active intermediates for O—O bond formation in the OER mechanism.

The Fe K-edge XANES spectra for CoFe, CFV33, and CFVv75 revealed significant electronic and structural transformations occurring during OER (Figure 5b). The initial edge energies were similar for all materials at OCP, with values of 7124.3, 7124.2, and 7124.5 eV for CoFe, CFV33, and CFVv75, respectively. These energies were comparable to the Fe_2O_3 reference, indicating predominantly Fe(III) species, in agreement with the XPS results (Figure S4, Supporting Information). Interestingly, a shift of 0.2 eV toward higher energies was observed only for CFVv75, indicating the further oxidation of Fe induced by the addition of 75 wt % $V_{1.8}CT_x$ MXene.

An increase in potential from $\eta = 0$ V to 0.3 V resulted in a gradual shift of all edge energies of the materials to higher energies, reaching a maximum at the 0.3 V. The only exception is CoFe, where no shift was observed up to 0.3 V, suggesting that the MXene incorporation facilitates an earlier transition of Fe, making it more susceptible to oxidation to higher oxidation states at lower potentials. Among the materials, CFV33 showed the most significant edge shift (ΔE_{Fe} of 1.4 eV), followed by CoFe (0.9 eV) and CFVv75 (0.7 eV), indicating the formation of iron species with oxidation states higher than +3 during the OER. As the potential continued to increase to 0.45 V, the edge energies started to decrease and shifted back to lower energies. Upon removal of the applied potential, both CFV33 and CFVv75 returned to their initial state. Interestingly, the shift in edge energies of CoFe shifted toward the edge energies of Fe_2O_3 reference, suggesting an oxidation state of +3. Although these energy shifts were less pronounced than those observed at the Co K-edge, comparison with the Fe_2O_3 reference suggests the formation of iron species with oxidation states higher than +3 during the OER. This observation corresponds with Reith et al.'s findings, where they detected iron oxidation states up to +3.2 in cobalt-iron oxyhydroxides during OER.[32] Furthermore, Fe(IV) and potentially higher oxidation states have been proposed as playing a crucial role for catalyzing the OER.[11,33] The increased presence of this catalytically active species may contribute to the observed shift in the rate-determining step from the second to the third partial reaction of OER, as indicated by the Tafel slope analysis.

The evolution of the local coordination structures of Fe atoms in CoFe, CFV33, and CFVv75 during OER was also investigated through the analysis of the Fourier transform of Fe K-edge EXAFS (S12b, d and f). The FT-EXAFS spectra of pure CoFe revealed significant changes in the local coordination environment around the Fe centers. Two overlapping peaks observed at 1.38 Å and 1.81 Å for CoFe at OCP conditions correspond to Fe—O bonds at different distances,[34] Upon increasing the applied potential from η = 0 V to 0.75 V, notable structural changes were observed in CoFe including a decrease in Fe—O bond length. The increased peak intensity and the merging of the two overlapping Fe-O peaks into a single peak with further increasing potential suggest changes in the structure. This increase in intensity may be attributed to the rise in the number of contributing Fe—O bonds during the OER process. The second coordination of pure CoFe at OCP exhibited two overlapping peaks observed at

© 2025 The Author(s). Advanced Functional Materials published by Wiley-VCH GmbH

16163028, 2026, 21, Downloaded from https://advanced.onlinelibrary.wiley.com/doi/10.1002/adfm.202503842 by Helmholtz-Zentrum Berlin Für, Wiley Online Library on [20/03/2026]. See the Terms and Conditions (https://onlinelibrary.wiley.com/terms-and-conditions) on Wiley Online Library for rules of use; OA articles are governed by the applicable Creative Commons License

2.59 and 2.99 Å, which could be attributed to the Fe/Co-Fe coordination. Fe-O-Co/Fe-Co and Fe-Fe, respectively.[35] While applying potential from 0 to 0.75 V, the intensity of the Fe-Fe peak diminished, and shifted to larger values, indicating an increase in the bond length, while the number of Fe—Co/Fe—O—Co bonds increased and formed more ordered structure.

Interestingly, the composites exhibited notably different local coordination structures. For instance, the Fe—O bonds in CFV33 at OCP were observed as a single peak. The Fe—O bond becomes stronger with applied potential, with a contraction from 1.51 to 1.34 Å from OCP to 0.75 V. When the potential returned to OCP, the bond length increased to 1.42 Å, which is very similar to that at 0.45 V. The second peak, corresponding to the Fe-Fe contribution, was observed to be shifted to smaller distances with applied potential compared to the FeO, Fe_2O_3 and Fe_3O_4 references. Furthermore, the Fe-Co peaks were not clearly observed, suggesting the formation of a small number of Fe—Co bonds when compared to the pure CoFe. These observations indicated that the addition of V_2CT_x to the CoFe induced the formation of more ordered Fe-O in the first shell and Fe–Fe interaction in the second shell with applied potential. Upon reverting to the OCP, a slight increase in the Fe—O bond and a reduction in the Fe-Fe intensity were observed, showing that the material retains some of the structures formed at elevated potentials. Very interestingly, the CFVv75 showed a combined pattern of pure CoFe and CFV33. The Fe-O peaks in the first shell exhibited broader shape, and the bond-length changes were less pronounced compared to the pure CoFe or CFV33 spectra. In the second shell, broad peaks with a shoulder appeared especially at 0.3 V and above, and at the final OCP state, which became stronger by following the same trend. This observation reveals an important difference with the CFV33, indicating the formation of Fe—Co bonds together with the Fe—Fe bonds, resulting in a facilitated electron transfer leading to a better OER activity. These results likely contributed to a favorable local coordination and electronic structure of the active sites in CFVv75, enhancing its catalytic activity.

XANES analysis of the V K-edge revealed significant electronic and structural changes during OER (Figure 5f). Ex-situ XAS measurements of the pure MXenes showed V_2CT_x aligned closely with VO_2 (V^{4+}) reference with an edge energy of 5477.9 eV, while $V_{1.8}CT_x$ exhibited a slightly higher energy position (5479.0 eV). The composite materials CFV33 and CFVv75 displayed higher V edge energies at OCP (5479.0 and 5479.6 eV, respectively), indicating partial oxidation of the MXene structure upon composite formation. During OER, these energies increased dramatically, with edge positions reaching 5483.6 and 5484.1 eV at $\eta = 0.45$ V for CFV33 and CFVv75, respectively. These substantial shifts are consistent with oxidation toward V^{5+} with significant changes in the local coordination environment, similar to observations in other vanadium-containing catalysts. Notably, these elevated edge energies persisted upon returning to OCP, indicating irreversible electronic structure modification of the vanadium centers.

The pre-edge features provided complementary insights into coordination changes (Figure 5c; Figure S11e,h, Supporting Information). At OCP and 0 V, both composite materials exhibited sharp, well-defined pre-edge peaks characteristic of their initial coordination state. With increasing potential (0.15 V), a noticeable decrease in edge intensity and broadening of the pre-edge peak emerged, becoming more pronounced at 0.45 V. The remarkable similarity between pre-edge features at 0.45 V and post-reaction OCP confirms the irreversible nature of these structural modifications. This evolution suggests a transformation from more octahedral-like coordination toward distorted or tetrahedral-like environments, potentially creating more catalytically active sites through modified V—O bonding. Together, these electronic and structural changes likely contribute to the enhanced OER performance observed in the composite materials, with the MXene component stabilizing the active vanadium species.

The combined analysis of Co, Fe, and V edges reveals intriguing relationships between the metal centers during the OER process. All three metal centers undergo oxidation during OER, but with distinctly different magnitudes and reversibility characteristics. The Co K-edge shows substantial shifts (3.2–3.3 eV) that remain after returning to OCP, while the Fe K-edge displays more modest shifts (0.4–1.1 eV) with CFV33 showing the largest change. The V K-edge exhibits the most dramatic and irreversible shifts (>4 eV), indicating complete oxidation from V^{4+} to V^{5+}. The irreversible nature of both Co and V oxidation suggests a permanent restructuring of the catalyst during the initial OER cycles, creating a more active phase that persists even after removing the applied potential. This behavior contrasts with the Fe centers, which show more reversible redox behavior according to the Fe K-edge analysis. The different roles of each metal appear complementary: Co centers likely provide the primary catalytic sites that undergo $Co^{2+} \rightarrow Co^{3+} \rightarrow Co^{4+}$ transitions during OER, Fe sites may facilitate electron transfer and modulate the electronic structure of neighboring Co atoms, while V centers contribute additional redox capacity and undergo irreversible structural transformation that enhances the overall stability of the catalyst. The particularly enhanced performance of the composite materials containing V-based MXene can be attributed to the synergistic interactions between these different metal centers. The irreversible oxidation of V to V^{5+} may create a more conducive electronic environment for stabilizing the catalytically active Co^{4+} species, while the presence of Fe lowers the energetic barrier for Co oxidation. This multi-metal cooperation provides a mechanistic explanation for the superior catalytic performance observed in the composite materials.

In conclusion, the XAS analysis reveals that the catalysts undergo significant electronic and structural modifications during OER, with the formation of high-valent metal species (Co^{4+}, Fe^{3+}, V^{5+}) playing crucial roles in the catalytic mechanism. The irreversible nature of these changes, particularly for Co and V centers, indicates that the catalyst evolves into a more active form during the initial OER cycles, with each metal serving a distinct but complementary function in the overall catalytic process. These findings highlight the importance of multi-metal synergy in designing high-performance OER catalysts and provide valuable insights for the rational development of more efficient and stable materials for water splitting applications.

2.4. Electrolyzer Device Measurements

Testing materials under realistic electrolyzer conditions is crucial for evaluating their practical applicability in industrial water splitting applications. Therefore, stability tests of the

© 2025 The Author(s). Advanced Functional Materials published by Wiley-VCH GmbH

16163028, 2026, 21, Downloaded from https://advanced.onlinelibrary.wiley.com/doi/10.1002/adfm.202503842 by Helmholtz-Zentrum Berlin Für, Wiley Online Library on [20/03/2026]. See the Terms and Conditions (https://onlinelibrary.wiley.com/terms-and-conditions) on Wiley Online Library for rules of use; OA articles are governed by the applicable Creative Commons License

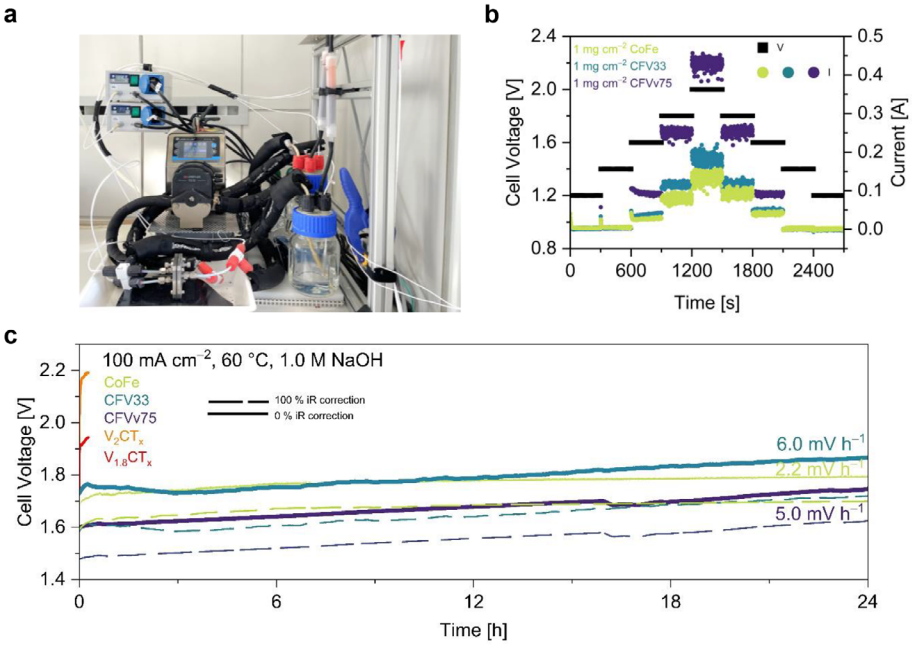

Figure 6. Electrolyzer device measurements. a) Image of the electrolyzer measurements setup. b) Activation of catalysts at various chronoamperometric steps at 60 °C. c) Chronopotentiometry of V_2CT_x, $V_{1.8}CT_x$, CoFe, CFV33, and CFVv75 at 100 mA cm^{-2} and 60 °C over 24 h.

best-performing materials were conducted in a complete electrolyzer setup (**Figure 6a**). The electrolyzer measurements revealed distinct performance characteristics among the tested materials at 60 °C. Before the stability tests, catalysts were activated by holding at various cell voltages each for 300 s (Figure 6b). The staircase testing with the CFVv75 catalyst demonstrated excellent activity, reaching ≈450 mA cm^{-2} at 2.0 V. In comparison, CFV33 achieved a maximum current density of 220 mA cm^{-2} at the same potential, surpassing the pure CoFe catalyst by 70 mA cm^{-2}.

For the stability tests at 100 mA cm^{-2} (Figure 6c), the CFV33 catalyst initially exhibited a cell voltage of 1.59 V, showing an activity close to pure CoFe, but exhibited a higher voltage increment of 6.0 mV h^{-1} compared to CoFe (2.2 mV h^{-1}). More promisingly, with a cell voltage of 1.48 V at 100 mA cm^{-2}, CFVv75 demonstrated superior performance, operating at a cell voltage 100 mV lower than pure CoFe at 100 mA cm^{-2}. Despite its higher voltage increase of 5.0 mV h^{-1} CFVv75 held a lower cell voltage over 24 h than CoFe. Additionally, CFVv75 exhibited the lowest series resistance among all tested catalysts (Figure S13b, Supporting Information). Furthermore, pure V_2CT_x and $V_{1.8}CT_x$ exhibited elevated cell voltages and faster degradation rates within a few minutes. This suggests that the incorporation of the CoFe catalyst not only stabilizes the MXenes but also enhances their activity for anion water electrolysis. In contrast, MXenes without the catalyst demonstrated a diminished activity.

Pre -and Post reaction XPS of the catalyst coated Ni-electrodes coincided with the results from the three-electrode stability tests discussed earlier (Figure S10c, Supporting Information). Briefly, the Co 2p spectra showed that cobalt had transformed from predominant Co(II) to Co(II/III) after OER in all three catalysts. The Fe 2p signal indicated that iron predominantly preserved its Fe(III) oxidation state. The V 2p spectra of both composites revealed that vanadium was initially present as V(V), but the signal completely disappeared after OER, suggesting significant V leaching.

Post-reaction ICP-OES analysis of the electrolytes from CFV33 and CFVv75 (Figure S13c, Supporting Information) revealed slightly higher V and significantly higher Fe leaching compared to the three-electrode cell stability tests (Figure S10, Supporting Information). This increased leaching likely contributes to the higher cell voltage increases observed in the composite materials. The elevated operating temperature of 60 °C in the electrolyzer versus room temperature in the three-electrode configuration may be responsible for increased leaching due to faster degradation kinetics. However, in the AEM cell, the CFVv75 materials shows less Fe leaching (Figure S13c, Supporting Information) and a slower degradation rate then the CFV33 which may suggest that $V_{1.8}CT_x$ is a better choice than V_2CT_x as a support for AEM water splitting.

Comparison of recently published cell voltages achieved at 100 mA cm^{-2} in membrane electrode assembly-based anion water electrolyzers (Table S1, Supporting Information) demonstrated CFVv75's superior performance to other MXene-based catalysts. These results confirm CFVv75 as a promising non-noble metal anode catalyst for sustainable hydrogen production, successfully translating its enhanced initial activity from fundamental electrochemical testing to practical electrolyzer conditions. Further investigation and optimization of the catalyst layer formulation and the electrolyzer experimental setup will be necessary to improve long-term performance stability.

3. Conclusion

This comprehensive investigation of $Co_{0.66}Fe_{0.34}$-LDH supported on vacancy-engineered MXenes has revealed several key insights into the design and optimization of OER electrocatalysts.

© 2025 The Author(s). Advanced Functional Materials published by Wiley-VCH GmbH

16163028, 2026, 21, Downloaded from https://advanced.onlinelibrary.wiley.com/doi/10.1002/adfm.202503842 by Helmholtz-Zentrum Berlin Für, Wiley Online Library on [20/03/2026]. See the Terms and Conditions (https://onlinelibrary.wiley.com/terms-and-conditions) on Wiley Online Library for rules of use; OA articles are governed by the applicable Creative Commons License

Through the variation of MXene content and the introduction of vanadium vacancies, we have demonstrated the significant impact of support material engineering on electrocatalytic performance.

The incorporation of both V_2CT_x and $V_{1.8}CT_x$ MXene supports led to enhanced catalytic activity compared to pure CoFe, with the vacancy-engineered $V_{1.8}CT_x$ composites showing superior performance. This enhancement is attributed to several factors elucidated through a multi-technique characterization approach. XRD analysis revealed the formation of a distinct LDH phase in the composite materials, facilitated by surface hydroxyl groups on the MXene support. The correlation between atomic ratios and catalytic activity identified optimal Co:Fe and V:CoFe compositions, with the vacancy-engineered materials showing enhanced performance at lower Co:Fe ratios.

In situ XAS measurements provided crucial insights into the evolution of the catalysts under operating conditions, revealing the formation of catalytically active Co (III) species and the irreversible oxidation of vanadium. Despite this structural change and partial vanadium leaching, both CFV33 and CFVv75 demonstrated remarkable stability during extended operation. Particularly noteworthy is the successful translation of the initial enhanced activity to practical electrolyzer conditions, where CFVv75 maintained significantly lower cell voltages compared to the pure CoFe catalyst. However, the MXene derived materials had a faster degradation rate in the AEM devices compared to the pure CoFe which will be further explored in future work.

These findings demonstrate the potential of vacancy engineering in MXene supports for enhancing electrocatalytic performance while also providing valuable insights into the complex interplay between support structure, composition, and catalytic activity. The understanding gained from this work opens new avenues for the rational design of high-performance electrocatalysts through strategic modification of support materials.

4. Experimental Section

Synthesis of Materials—Synthesis of V_2AlC MAX Phase: Stoichiometric amounts of powdered graphite (99.999%, Sigma–Aldrich), V (99.99%, Sigma–Aldrich), and Al (99.8%, Alfa Aesar) were mixed in an agate mortar. The mixed powder was heated to 1550 °C for 2 h in an alumina crucible under flowing argon. After cooling down to RT in the furnace, a loosely packed powder was obtained. The powder was crushed and sieved through a 450 mesh sieve (particle size ≈32 µm).

Synthesis of Materials—Synthesis of $V_{1.8}Cr_{0.2}AlC$ MAX Phase: Stoichiometric amounts of powdered graphite (99.999%, Sigma–Aldrich), V (99.99%, Sigma–Aldrich), Cr (99.99%, Sigma–Aldrich), and Al (99.8%, Alfa Aesar) were mixed in an agate mortar, heated to 1450 °C in an alumina crucible under flowing argon and held at that temperature for 10 h. A loosely packed powder was obtained after cooling down to RT in the furnace. The powder was crushed and sieved through a 450 mesh sieve (particle size ≈32 µm).

Synthesis of Materials—Preparation of V_2CT_x and $V_{1.8}CT_x$ MXene: For the synthesis of V_2CT_x, V_2AlC (2 g, 450 mesh) was slowly added to 48% HF (20 mL) solution with stirring, after which the mixture was stirred for 72 h at 40 °C. The dispersion was then centrifuged at 6000 rpm for 5 min to harvest the sediment, which was further centrifuged and washed with deionized (DI) water until the pH value reached ≈6. The produced multilayered MXene was delaminated via intercalation by adding TBAOH (40% in H_2O, Sigma–Aldrich), which was then manually shaken for ≈5 min. The solution was put in the centrifuge for another 5 min at 6000 rpm and was rinsed with DI water three times without shaking to remove any TBAOH residues. Finally, the intercalated MXene powders was mixed with DI water (30 mL), manually shaken for 10 min, and then centrifuged at 3000 rpm for 30 min. The high-quality delaminated MXene suspension was decanted gently by excluding the sediment.

The synthesis of $V_{1.8}CT_x$ was similar to that of V_2CT_x, except for the etching time and temperature. $V_{1.8}Cr_{0.2}AlC$ was etched at 35 °C for 48 h to provide $V_{1.8}CT_x$. For further details see previous work.[21]

Synthesis of Materials—Preparation of CFV and CFVv Composites: In a typical synthesis, $Co(NO_3)_2{\cdot}6H_2O$ (192.1 mg, 0.66 mmol, 99.99%, Sigma–Aldrich) and $Fe(NO_3)_3{\cdot}9H_2O$ (137.4 mg, 0.34 mmol, 99.99%, Sigma–Aldrich) were combined with urea (300.3 mg, 5.0 mmol, 99.0-100.5%, Sigma–Aldrich) in a 20 mL crimp-top vial. V_2CT_x or $V_{1.8}CT_x$ dispersion amounting to 18.8, 45.3, 91.0 and 275.7 mg of MXene was added to achieve MXene: $(Co_{0.66}Fe_{0.34}(OH)_2$+MXene) ratios of 17, 33, 50, and 75 wt.% in the final product. The V_2CT_x containing materials were labeled CFV17,-33,-50,-75 and the $V_{1.8}CT_x$ containing materials were labeled CFVv17,-33,-50,-75 according to their targeted MXene wt.% throughout this work. The mixture was diluted with DI water to a volume of 5 mL, followed by the addition of N-methyl-2-pyrrolidone (5 mL). The vial was sealed with a membrane cap and saturated with N_2 for 15 min. The reaction mixture was then heated to 100 °C in an oil bath and magnetically stirred at that temperature for 5 h. After cooling naturally to room temperature, the product was isolated by centrifugation and purified through successive washing steps with deionized water (3x) and ethanol (1x), with the supernatant being discarded after each centrifugation cycle. The final product was dried at 60 °C for 12 h.

Synthesis of Materials—Preparation of Reference Materials: The pure CoFe reference material was synthesized following the same procedure without the addition of MXene dispersion. Reference materials were prepared similarly, with 45.3 mg V_2AlC, 275.7 mg $V_{1.8}Cr_{0.2}AlC$, and 45.3 and 275.7 mg carbon black substituted for the MXene dispersion respectively and were named CFMAX33, CFMAXv75, CFCB33 and CFCB75 accordingly. Physically mixed reference samples were prepared by mixing dispersions of pure CoFe and MXenes amounting to 33 wt.% V_2CT_x and 75 wt.% $V_{1.8}CT_x$ in the dried mixture respectively and were named PMV33 and PMVv75.

Materials Characterization: ICP-OES measurements were performed using an iCAP 7400 Duo Full MFC device (Thermo Fisher Scientific) in axial mode. X-ray diffractograms were recorded using a Bruker D8 ADVANCE powder diffractometer using Cu Kα1 ($\lambda = 0.1541$ nm), and Kα2 radiation source ($\lambda = 0.1544$ nm). Diffraction patterns were collected between 5° and 110° applying a step size of 0.0131° and a step time of 1.25 s. Scanning electron micrographs were obtained on a Zeiss MERLIN 0.1–30 keV field emission gun scanning electron microscopes. Samples were prepared by spreading the relevant material onto adhesive carbon tape on top of an aluminum specimen holder. XPS measurements were conducted using a JEOL JPS-9030 setup with a base pressure of $2 \cdot 10^{-9}$ mbar. The powders were evenly distributed on carbon tape for the measurements. Both non-monochromated Al and Mg sources with 300 W power were used for excitation to distinguish overlapping Auger peaks. A hemispherical analyzer with pass energy of 50 eV (surveys) and 20 eV (narrow scans) was used to detect the emitted photoelectrons, yielding a resolution of 1.0–1.1 eV. The binding energy scale of the analyzer was calibrated by setting the Au 4f7/2 and the Cu 2p3/2 peaks of clean gold and copper foils to 84.0 and 932.6 eV, respectively. However, since the samples showed charging, it shifted the binding energy of the C—C peak of the carbon tape to 285.0 eV for comparison. Sensitivity factors were calculated using the experimentally determined transmission function of the analyzer, the atomic cross sections after Scofield[36] and the inelastic mean free path for elements given by Seah and Dench.[37] TEM imaging was conducted on a FEI Titan 80–300 microscope (Thermo Fisher Scientific), equipped with a Schottky field emission gun. The system was operated at 300 kV, and images were captured using a Gatan UltraScan CCD camera. Elemental analysis was carried out with Energy Dispersive X-Ray Spectroscopy (EDS) using a Bruker XFlash 6–30 EDS detector. Elemental mapping was performed in STEM mode, employing a HAADF detector. The samples were dispersed in isopropanol and drop-cast onto lacey carbon grids for imaging. X-ray absorption

© 2025 The Author(s). Advanced Functional Materials published by Wiley-VCH GmbH

16163028, 2026, 21, Downloaded from https://advanced.onlinelibrary.wiley.com/doi/10.1002/adfm.202503842 by Helmholtz-Zentrum Berlin Für, Wiley Online Library on [20/03/2026]. See the Terms and Conditions (https://onlinelibrary.wiley.com/terms-and-conditions) on Wiley Online Library for rules of use; OA articles are governed by the applicable Creative Commons License

16163028, 2026, 21, Downloaded from https://advanced.onlinelibrary.wiley.com/doi/10.1002/adfm.202503842 by Helmholtz-Zentrum Berlin Für, Wiley Online Library on [20/03/2026]. See the Terms and Conditions (https://onlinelibrary.wiley.com/terms-and-conditions) on Wiley Online Library for rules of use; OA articles are governed by the applicable Creative Commons License

spectroscopy (XAS) measurements were performed at the SAMBA beamline at SOLEIL synchrotron, France. Working electrodes (WE) were prepared by drop-casting a dispersion of the catalyst material onto a flexible graphite foil support, followed by drying on a hot plate at 60 °C. The XAS measurements were conducted in a custom-built three-electrode cell equipped with the as prepared WE, a Pt wire counter electrode (CE), and a Hg/HgO reference electrode (RE). Fluorescence spectra were collected at a 45° angle relative to the WE surface at the Co, Fe, and V K-edges. Energy calibration was performed using the corresponding metal foils (Co, Fe, and V) as references Typically, ex situ XAS spectra of catalysts and references were initially obtained of the samples in the three-electrode cell. Subsequently, the cell was filled with N_2-purged 1 M NaOH, and XAS spectra were collected at OCP. Chronoamperometry measurements were then performed at successive potentials of 0.3, 0.45, 0.6, and 0.75 V versus Hg/HgO, with XAS spectra collected during each potential step. Finally, the samples were characterized again at OCP. Data analysis was conducted using the software Fastosh v1.0.8. The edge positions in the X-ray absorption near-edge structure (XANES) spectra were determined using the half-edge step method.[38] Adsorption-desorption isotherms were obtained by Nitrogen physisorption using Quantachrome Autosorb-1 systems performed at 77 K. The samples were prior degassed at 120 °C for 20 h using a built-in outgasser station, then refilled with the absorbate to nearly ambient pressure. Zeta potentials were measured with a Malvern Panalytical Zetasizer Nano ZS. Dispersions containing 0.5 g L^{-1} in a 1:1 mixture of DI water and isopropanol were sonicated for 30 min before injecting it into a disposable folded capillary cell (Malvern). For each sample the average of 3 zeta potential measurements was taken.

Electrochemical Characterization: Three electrode experiments were conducted using a CHI760E potentiostat and a standard three-electrode cell consisting of a Hg/HgO RE a carbon rod as the CE and a glassy carbon (GC) rotating disk electrode (RDE) with an electrode area of 0.0707 cm^2 as WE, which was polished using a 0.05 µm alumina polish before use. 1.13 µL of an ink dispersion made up of 10 mg of the relevant catalyst material in 496 µL of H_2O, 496 µL of isopropanol and 8 µL of Nafion solution was drop cast onto the GC electrode and dried under a gentle nitrogen stream, resulting in a catalyst loading of 0.16 mg cm^{-2}. The electrodes were immersed into a nitrogen-saturated 1 M NaOH electrolyte solution which was prepared using DI water with a resistivity of 18.2 MΩ cm (Barnstead Smart2Pure Pro Water Purification System, Thermo Scientific). The potentials measured versus Hg/HgO were mathematically converted to overpotential η using the equation $E = E_{Hg/HgO} + 0.059\ pH + E^0_{Hg/HgO} + E^0$, where $E_{Hg/HgO}$ is the standard Hg/HgO electrode potential equal to 0.098 V at 25 °C and E^0 was the standard cell potential of OER and was equal to 1.23 V. Unless otherwise specified, the WE was rotated at 1600 rpm during all RDE measurements. Routinely before other measurements, chronopotentiometry was conducted at a constant current of 10 mA cm^{-2} for 60 s or until the potential stabilized. For measuring the charge transfer resistance (R_{ct}) during the OER, galvanostatic electrochemical impedance spectroscopy (EIS) was conducted at a current of 10 mA cm^{-2} in a frequency range of 0.1–10^5 Hz. Potentiostatic EIS was conducted at subsequent applied potentials of 1.50, 1.55, 1,60 and 1.65 V versus RHE in a frequency range of 0.1–10^5 Hz. Nyquist plots were corrected for the electrode-specific series resistance R_s. Linear sweep voltammetry (LSV) measurements were conducted at a scan rate of 1 mV s^{-1} and cyclic voltammetry at a scan rate of 40 mV s^{-1}. Polarization curves were IR-drop corrected by the automatic IR correction of the potentiostat. Electrical double layer capacitance was measured by running multiple CVs over a scan range of 100 mV with the scan rate ranging from 1 to 100 mV s^{-1}. The respective currents measured in a non-Faradaic region of the scan range were then plotted against the scan rate and the double layer capacitance C_{dl} was determined from the slope of this plot. ECSA was calculated by dividing C_{dl} by the material's specific capacitance C_F which for transition metals in 1 M NaOH was 0.04 mF cm^{-2}.[39] The mean overpotential at 10 mA cm^{-2} (η_{10}) was calculated from at least three independent electrode measurements per material. For electrocatalytic stability tests, chronopotentiometry was conducted at a constant current of 100 mA cm^{-2} for 12 h. As WE, a 1.0 cm^2 nickel fiber felt (35 µm fiber diameter, 0.5 mm thickness, 80% porosity, Xinxiang Aida Machinery Equipment Corporation, China) was used. Nickel fiber felts were cleaned by sonicating in 20% HCl for 20 min followed by sonicating subsequently in DI water, acetone, isopropanol, ethanol and DI water for 10 min each, before being spray coated with 1.0 mg of catalytic material.

Single cell electrolyzer measurements were conducted using a Parstat 4000+ potentiostat (AMETEK, Inc.) in an in-house developed 1.0 cm^2 area flow field cell. For these measurements, 0.5 mm thick ethylene propylene diene monomer gaskets were used, and a bolt torque of 1.0 N m was applied to ensure zero-leak, and a low series contact resistance between the flow fields and the electrodes. Fumasep FAA-3–50 (45–55 µm thickness, Fumatech BWT GmbH) anion exchange membranes (AEM) were used as ion conducting separator and were activated by soaking them in nitrogen saturated 1 M NaOH for at least 24 h before the single-cell measurements. A two-channel peristaltic pump from Redox-Flow was used to feed the electrolyte at a flow rate of 50 mL min^{-1}. For the cathode, catalyst suspension consisting of 14 mg Pt/C (Platinum, nominally 40% on carbon black), 750 µL isopropanol, 50 µL Fumion ionomer (10% Fumion solution) and 200 µL DI water. The suspension was sprayed to a 1.0 cm^2 cleaned nickel fiber felt using an air gun, reaching a platinum loading of 0.5 mg cm^{-2}. For the anode, a 1.0 cm^2 nickel fiber felt was spray coated with 1.0 mg of catalytic material. Before applying constant current density of 100 mA cm^{-2} to the electrolyzer cell, the catalysts were activated with multiple voltage steps by holding at 1.2 V, 1.4 V, 1.6 V, 1.8 V, 2.0 V, and back to 1.2 V for 5 min each.

Supporting Information

Supporting Information is available from the Wiley Online Library or from the author.

Acknowledgements

The authors gratefully acknowledge the Helmholtz Association's Initiative and Networking Fund (Helmholtz Young Investigator Group VH-NG-1719) for the funding. M.P.B greatly acknowledges support from the German Federal Ministry of Education and Research in the framework of the project Catlab (03EW0015A/B). V.N. wishes to acknowledge funding from the European Research Council (CoG 3D2Dprint, GA 681544), Science Foundation Ireland (12/RC/2278_P2 and 16/RC/3872_P2, Frontiers for the Future 20/FFP-A/8950), and HORIZON-RIA 101091572 GREENCAP. DDH would like to thank the SFI-funded CRANN Advanced Microscopy Laboratory (AML) for the provision of their facilities for the electron microscopy characterization and analysis. J.R. acknowledges funding from the European Research Council (CoG MULTI2D), from the Knut and Alice Wallenberg (KAW) Foundation for a Scholar grant and Project funding (2020.0033) and from the Swedish Government Strategic Research Area in Materials Science on Advanced Functional Materials at Linköping University (Faculty Grant SFO-Mat-LiU No. 2009-00971). The authors would like to address particular thanks to R. Schwiddessen, M. Tovar and K. Schwarzburg from the X-Ray and Microscopy and Spectroscopy Corelabs of the Helmholtz Zentrum Berlin for providing access to their facility and training on the equipment. The ICP-OES measurements were carried out by the "Solar Fuels Testing Facility" laboratory of the Helmholtz Energy Materials Foundry (HEMF). The authors acknowledge SOLEIL for provision of synchrotron radiation facilities through Grant No. 20231879 and 20240005. Open Access funding enabled and organized by Pro jekt DEAL.

Open access funding enabled and organized by Projekt DEAL.

Conflict of Interest

The authors declare no conflict of interest.

Data Availability Statement

The data that support the findings of this study are available from the corresponding author upon reasonable request.

© 2025 The Author(s). Advanced Functional Materials published by Wiley-VCH GmbH

Keywords

anion exchange membrane electrolyzers, cobalt-iron layered double hydroxides, electrocatalysis, in situ XAS, MXenes, oxygen evolution reaction, vacancy engineering

Received: February 11, 2025
Revised: April 23, 2025
Published online: May 15, 2025

[1] M. Yu, E. Budiyanto, H. Tüysüz, *Angew. Chem., Int. Ed.* **2022**, *61*, 202103824.
[2] a) S. Lee, A. Moysiadou, Y.-C. Chu, H. M. Chen, X. Hu, *Energy Environ. Sci.* **2022**, *15*, 206; b) P. Babar, A. Lokhande, H. H. Shin, B. Pawar, M. G. Gang, S. Pawar, J. H. Kim, *Small* **2018**, *14*, 1702568; c) M. S. Burke, M. G. Kast, L. Trotochaud, A. M. Smith, S. W. Boettcher, *J. Am. Chem. Soc.* **2015**, *137*, 3638; d) E. Budiyanto, S. Salamon, Y. Wang, H. Wende, H. Tüysüz, *JACS Au* **2022**, *2*, 697; e) L. Bai, C.-S. Hsu, D. T. L. Alexander, H. M. Chen, X. Hu, *J. Am. Chem. Soc.* **2019**, *141*, 14190; f) Q. Qian, Y. Li, Y. Liu, G. Zhang, *Appl. Catal., B* **2020**, *266*, 118642.
[3] M. E. G. Lyons, M. P. Brandon, *J. Electroanal. Chem.* **2010**, *641*, 119.
[4] a) L. Yan, Z. Du, X. Lai, J. Lan, X. Liu, J. Liao, Y. Feng, H. Li, *Int. J. Hydrogen Energy* **2023**, *48*, 1892; b) J. Jiang, A. Zhang, L. Li, L. Ai, *J. Power Sources* **2015**, *278*, 445; c) F. Dionigi, P. Strasser, *Adv. Energy Mater.* **2016**, *6*, 1600621; d) F. Dionigi, Z. Zeng, I. Sinev, T. Merzdorf, S. Deshpande, M. B. Lopez, S. Kunze, I. Zegkinoglou, H. Sarodnik, D. Fan, *Nat. Commun.* **2020**, *11*, 2522; e) X. Teng, D. Si, L. Chen, J. Shi, *eScience* **2024**, *4*, 100272.
[5] G. Fan, F. Li, D. G. Evans, X. Duan, *Chem. Soc. Rev.* **2014**, *43*, 7040.
[6] Y. Wang, D. Yan, S. El Hankari, Y. Zou, S. Wang, *Adv. Sci.* **2018**, *5*, 1800064.
[7] F. Song, L. Bai, A. Moysiadou, S. Lee, C. Hu, L. Liardet, X. Hu, *J. Am. Chem. Soc.* **2018**, *140*, 7748.
[8] a) M. Gong, Y. Li, H. Wang, Y. Liang, J. Z. Wu, J. Zhou, J. Wang, T. Regier, F. Wei, H. Dai, *J. Am. Chem. Soc.* **2013**, *135*, 8452; b) G. Li, Y. Tang, T. Fu, Y. Xiang, Z. Xiong, Y. Si, C. Guo, Z. Jiang, *Chem. Eng. J.* **2022**, *429*, 132174; c) Y. Liu, L. Bai, T. Li, H. Liu, X. Wang, L. Zhang, X. Hao, C. He, S. Guo, *Mater. Adv.* **2022**, *3*, 4359.
[9] a) J. Dong, S. Wang, P. Xi, X. Zhang, X. Zhu, H. Wang, T. Huang, *Nanomaterials* **2023**, *13*, 2735; b) I. Madakannu, I. Patil, B. A. Kakade, K. R. D. Kasibhatta, *Mater. Chem. Phys.* **2020**, *252*, 123238.
[10] a) A. Kostuch, J. Gryboś, S. Wierzbicki, Z. Sojka, K. Kruczała, *Materials* **2021**, *14*, 820; b) M. Shen, C. Ruan, Y. Chen, C. Jiang, K. Ai, L. Lu, *ACS Appl. Mater. Interfaces* **2015**, *7*, 1207.
[11] M. Görlin, J. Ferreira de Araújo, H. Schmies, D. Bernsmeier, S. Dresp, M. Gliech, Z. Jusys, P. Chernev, R. Kraehnert, H. Dau, P. Strasser, *J. Am. Chem. Soc.* **2017**, *139*, 2070.
[12] A. VahidMohammadi, J. Rosen, Y. Gogotsi, *Science* **2021**, *372*, abf1581.
[13] a) A. K. S Navjyoti, V. Sharma, A. K. Debnath, V. Saxena, A. Mahajan, *J. Alloys Compd.* **2023**, *939*, 168779; b) D. Vikraman, S. Hussain, L. Hailiang, K. Karuppasamy, P. Sivakumar, P. Santhoshkumar, J. Jung, H.-S. Kim, *Inorg. Chem. Front.* **2022**, *9*, 5903; c) M. Alhabeb, K. Maleski, B. Anasori, P. Lelyukh, L. Clark, S. Sin, Y. Gogotsi, *Chem. Mater.* **2017**, *29*, 7633.
[14] J. L. Hart, K. Hantanasirisakul, A. C. Lang, B. Anasori, D. Pinto, Y. Pivak, J. T. van Omme, S. J. May, Y. Gogotsi, M. L. Taheri, *Nat. Commun.* **2019**, *10*, 522.
[15] a) Y. Lu, D. Fan, Z. Chen, W. Xiao, C. Cao, X. Yang, *Sci. Bull.* **2020**, *65*, 460; b) L. Yu, L. Lu, X. Zhou, L. Xu, *Adv. Mater. Interfaces* **2023**, *10*, 2201818; c) H. Huang, B. Shen, M. Yan, H. He, L. Yang, Q. Jiang, G. Ying, *Fuel* **2022**, *328*, 125234; d) S. Ghorbanzadeh, S. A. Hosseini, M. Alishahi, *J. Alloys Compd.* **2022**, *920*, 165811; e) M. Buldu-Akturk, T. Schultz, N. Sharma, U. Michalczik, P. Bogdanoff, N. Koch, M. P. Browne, *Electrochim. Acta* **2025**, *513*, 145529; f) J. Sheng, J. Kang, P. Jiang, K. Meinander, X. Hong, H. Jiang, Nonappa, O. I, H. P. Komsa, B. Peng, Z. P. Lv, *Small* **2025**, *21*, 2404927; g) L. Hu, R. Xiao, X. Wang, X. Wang, C. Wang, J. Wen, W. Gu, C. Zhu, *Appl. Catal., B* **2021**, *298*, 120599.
[16] C. Kaplan, R. M. Restrepo, T. Schultz, K. Li, V. Nicolosi, N. Koch, M. P. Browne, *Electrochim. Acta* **2024**, *490*, 144269.
[17] C. Hao, Y. Wu, Y. An, B. Cui, J. Lin, X. Li, D. Wang, M. Jiang, Z. Cheng, S. Hu, *Mater. Today Energy* **2019**, *12*, 453.
[18] a) X. Zhao, X. Zheng, Q. Lu, Y. Li, F. Xiao, B. Tang, S. Wang, D. Y. W. Yu, A. L. Rogach, *EcoMat* **2023**, *5*, 12293; b) B. Schmiedecke, B. Wu, T. Schultz, A. A. Emerenciano, N. Sharma, D. A. Douglas-Henry, A. Koutsioukis, M. T. Görüryılmaz, V. Nicolosi, T. Petit, N. Koch, Z. Sofer, M. P. Browne, *J. Mater. Chem. A* **2024**, *12*, 24248; c) C.-H. Lin, S. Perumal, Y.-C. Lin, L.-Y. Hsiao, L.-Y. Lin, K.-C. Ho, *Int. J. Hydrogen Energy* **2025**, *111*, 40.
[19] B. Schmiedecke, B. Wu, T. Schultz, N. Koch, Z. Sofer, M. P. Browne, *ChemRxiv* **2025**, https://doi.org/10.26434/chemrxiv-2025-0pbfs.
[20] a) S. Ram, G. H. Choi, A. S. Lee, S.-C. Lee, S. Bhattacharjee, *J. Phys. Chem. C* **2023**, *127*, 12576; b) C. Wang, X. Hai, H. Wang, Y. Song, Z. Wan, Y. Yang, P. Huai, Y.-R. Yin, *J. Phys. Chem. C* **2024**, *128*, 10324; c) J. Gan, F. Li, Q. Tang, *J. Phys. Chem. Lett.* **2021**, *12*, 4805; d) Y. Tang, C. Yang, X. Xu, Y. Kang, J. Henzie, W. Que, Y. Yamauchi, *Adv. Energy Mater.* **2022**, *12*, 2103867; e) M. Zhang, H. Yin, F. Jin, J. Liu, X. Ji, A. Du, W. Yang, Z. Liu, *Green Energy Environ.* **2023**, *8*, 1185; f) R. M. Ronchi, J. Halim, N. Chen, P. O. Å. Persson, J. Rosen, *Small Science* **2024**, *4*, 2400204; g) Y. Li, W. Wang, M. Cheng, Y. Feng, X. Han, Q. Qian, Y. Zhu, G. Zhang, *Adv. Mater.* **2023**, *35*, 2206351.
[21] L. Qin, R. Samal, J. Jiang, J. Halim, N. Chen, F. Chabanais, P. O. A. Persson, J. Rosen, *arXiv* **2025**, https://doi.org/10.48550/ARXIV.2505.04226.
[22] S. Intikhab, V. Natu, J. Li, Y. Li, Q. Tao, J. Rosen, M. W. Barsoum, J. Snyder, *J. Catal.* **2019**, *371*, 325.
[23] M. C. Biesinger, B. P. Payne, A. P. Grosvenor, L. W. Lau, A. R. Gerson, R. S. C. Smart, *Appl. Surf. Sci.* **2011**, *257*, 2717.
[24] a) A. R. Chourasia, S. Islam, E. Aloyine, P. Adhikari, *Surface Science Spectra* **2024**, *31*, 014008; b) The International XPS Database, Cobalt (Co) Compounds, Cobalt Hydroxide (Co(OH)2) **2018**, https://xpsdatabase.net/cobalt-spectra-cooh2, (accessed: 2025).
[25] T. Yamashita, P. Hayes, *Appl. Surf. Sci.* **2008**, *254*, 2441.
[26] E. P. Alsaç, M. Boke, J. R. Bissonnette, R. D. Smith, *Chem. Sci.* **2024**, *15*, 15339.
[27] K. Fan, H. Chen, Y. Ji, H. Huang, P. M. Claesson, Q. Daniel, B. Philippe, H. Rensmo, F. Li, Y. Luo, L. Sun, *Nat. Commun.* **2016**, *7*, 11981.
[28] R. L. Doyle, M. E. G. Lyons, *J. Electrochem. Soc.* **2013**, *160*, H142.
[29] A. Chourasia, S. Islam, E. Aloyine, P. Adhikari, *Surface Science Spectra* **2024**, *31*, 014008.
[30] a) Z. Chen, N. Han, R. Zheng, Z. Ren, W. Wei, B.-J. Ni, *SusMat* **2023**, *3*, 290; b) W. Liu, H. Liu, L. Dang, H. Zhang, X. Wu, B. Yang, Z. Li, X. Zhang, L. Lei, S. Jin, *Adv. Funct. Mater.* **2017**, *27*, 1603904; c) S. Yan, M. Zhong, C. Wang, X. Lu, *Chem. Eng. J.* **2022**, *430*, 132955; d) X. Yi, X. He, F. Yin, B. Chen, G. Li, H. Yin, *Dalton Trans.* **2020**, *49*, 6764.
[31] Y. Zhao, N. Dongfang, C. Huang, R. Erni, J. Li, H. Zhao, L. Pan, M. Iannuzzi, G. R. Patzke, *Nat. Commun.* **2025**, *16*, 580.
[32] L. Reith, J. N. Hausmann, S. Mebs, I. Mondal, H. Dau, M. Driess, P. W. Menezes, *Adv. Energy Mater.* **2023**, *13*, 2203886.
[33] M. Görlin, P. Chernev, J. F. de Araújo, T. Reier, *J. Am. Chem. Soc* **2016**, *138*, 5603.
[34] Y. Zhao, N. Dongfang, C. Huang, R. Erni, J. Li, H. Zhao, L. Pan, M. Iannuzzi, G. R. Patzke, *Nat. Commun.* **2025**, *16*, 580.

© 2025 The Author(s). Advanced Functional Materials published by Wiley-VCH GmbH

16163028, 2026, 21, Downloaded from https://advanced.onlinelibrary.wiley.com/doi/10.1002/adfm.202503842 by Helmholtz-Zentrum Berlin Für, Wiley Online Library on [20/03/2026]. See the Terms and Conditions (https://onlinelibrary.wiley.com/terms-and-conditions) on Wiley Online Library for rules of use; OA articles are governed by the applicable Creative Commons License

[35] a) M. Cai, S. Sun, J. Bao, *ChemPhysChem* **2024**, *25*, 202300939; b) H. Li, C. Tian, L. Wang, Y. Mo, J. Li, C. Wang, C. Li, L. Zheng, F. Huang, Q. Li, *Mater. Today Energy* **2023**, *35*, 101307.
[36] J. H. Scofield, Theoretical photoionization cross sections from 1 to 1500 keV, Office of Scientific and Technical Information (OSTI) **1973**, https://doi.org/10.2172/4545040.
[37] M. P. Seah, W. Dench, *Surf. Interface Anal.* **1979**, *1*, 2.
[38] J. Wang, C.-S. Hsu, T.-S. Wu, T.-S. Chan, N.-T. Suen, J.-F. Lee, H. M. Chen, *Nat. Commun.* **2023**, *14*, 6576.
[39] C. C. L. McCrory, S. Jung, J. C. Peters, T. F. Jaramillo, *J. Am. Chem. Soc.* **2013**, *135*, 16977.

© 2025 The Author(s). Advanced Functional Materials published by Wiley-VCH GmbH

16163028, 2026, 21, Downloaded from https://advanced.onlinelibrary.wiley.com/doi/10.1002/adfm.202503842 by Helmholtz-Zentrum Berlin Für, Wiley Online Library on [20/03/2026]. See the Terms and Conditions (https://onlinelibrary.wiley.com/terms-and-conditions) on Wiley Online Library for rules of use; OA articles are governed by the applicable Creative Commons License